



AFRL-AFOSR-VA-TR-2016-0336

Airborne Aero-Optics Laboratory - Transonic (AAOL-T)

**Eric Jumper
UNIVERSITY OF NOTRE DAME DU LAC
940 GRACE HALL
NOTRE DAME, IN 465565602**

**10/17/2016
Final Report**

DISTRIBUTION A: Distribution approved for public release.

Air Force Research Laboratory
AF Office Of Scientific Research (AFOSR)/RTB1

REPORT DOCUMENTATION PAGE					Form Approved OMB No. 0704-0188	
<p>The public reporting burden for this collection of information is estimated to average 1 hour per response, including the time for reviewing instructions, searching existing data sources, gathering and maintaining the data needed, and completing and reviewing the collection of information. Send comments regarding this burden estimate or any other aspect of this collection of information, including suggestions for reducing the burden, to the Department of Defense, Executive Service Directorate (0704-0188). Respondents should be aware that notwithstanding any other provision of law, no person shall be subject to any penalty for failing to comply with a collection of information if it does not display a currently valid OMB control number.</p>						
PLEASE DO NOT RETURN YOUR FORM TO THE ABOVE ORGANIZATION.						
1. REPORT DATE (DD-MM-YYYY) 03-10-2016		2. REPORT TYPE Final Performance Report		3. DATES COVERED (From - To) Oct 2012-Oct 2015		
4. TITLE AND SUBTITLE Airborne Aero-Optics Laboratory - Transonic (AAOL-T)			5a. CONTRACT NUMBER FA9550-13-1-0001			
			5b. GRANT NUMBER			
			5c. PROGRAM ELEMENT NUMBER			
6. AUTHOR(S) Dr. Eric J. Jumper			5d. PROJECT NUMBER			
			5e. TASK NUMBER			
			5f. WORK UNIT NUMBER			
7. PERFORMING ORGANIZATION NAME(S) AND ADDRESS(ES) DR. ERIC J. JUMPER UNIVERSITY OF NOTRE DAME 301 CUSHING HALL NOTRE DAME, IN 46556-5612				8. PERFORMING ORGANIZATION REPORT NUMBER		
9. SPONSORING/MONITORING AGENCY NAME(S) AND ADDRESS(ES) Dr. John Luginsland Air Force Office of Scientific Research 875 N. Randolph Arlington, VA 22203				10. SPONSOR/MONITOR'S ACRONYM(S)		
				11. SPONSOR/MONITOR'S REPORT NUMBER(S)		
12. DISTRIBUTION/AVAILABILITY STATEMENT DISTRIBUTION A: Distribution approved for public release.						
13. SUPPLEMENTARY NOTES						
14. ABSTRACT This report covers the third year of the Airborne Aero-Optics Laboratory-Transonic (AAOL-T) program. Aero-optics severely limits an airborne directed-energy system's lethal field of regard; aero-optics refers to the deleterious effect that the density fluctuations in the flow have on an airborne optical system. The AAOL-T program studies aero-optical aberration problems from experimental, theoretical and computational approaches; the most unique part of the program is that we also perform flight tests using Falcon 10's, capable of testing at greater than Mach 0.8. The program makes use of two aircraft, one to project a small-aperture, diverging beam toward an optical turret on the second, laboratory aircraft. The third year of the program has been productive with thirty-one flights flown in support of both the baseline program and to support AFRL/DARPA 40% ABC Turret testing, of which 5 flights plus seven at the end of September 2014 were under the baseline program. During the baseline program, extensive measurements of aero-optical environment around both hemisphere-on-cylinder and hemisphere-only turrets were performed for Mach range between 0.5 and 0.8.						
15. SUBJECT TERMS						
16. SECURITY CLASSIFICATION OF: a. REPORT Unclassified		17. LIMITATION OF ABSTRACT b. ABSTRACT Unclassified c. THIS PAGE Unclassified		18. NUMBER OF PAGES UU 33	19a. NAME OF RESPONSIBLE PERSON Philp Rollins 19b. TELEPHONE NUMBER (Include area code) 574-631-3755	

INSTRUCTIONS FOR COMPLETING SF 298

- 1. REPORT DATE.** Full publication date, including day, month, if available. Must cite at least the year and be Year 2000 compliant, e.g. 30-06-1998; xx-06-1998; xx-xx-1998.
- 2. REPORT TYPE.** State the type of report, such as final, technical, interim, memorandum, master's thesis, progress, quarterly, research, special, group study, etc.
- 3. DATES COVERED.** Indicate the time during which the work was performed and the report was written, e.g., Jun 1997 - Jun 1998; 1-10 Jun 1996; May - Nov 1998; Nov 1998.
- 4. TITLE.** Enter title and subtitle with volume number and part number, if applicable. On classified documents, enter the title classification in parentheses.
- 5a. CONTRACT NUMBER.** Enter all contract numbers as they appear in the report, e.g. F33615-86-C-5169.
- 5b. GRANT NUMBER.** Enter all grant numbers as they appear in the report, e.g. AFOSR-82-1234.
- 5c. PROGRAM ELEMENT NUMBER.** Enter all program element numbers as they appear in the report, e.g. 61101A.
- 5d. PROJECT NUMBER.** Enter all project numbers as they appear in the report, e.g. 1F665702D1257; ILIR.
- 5e. TASK NUMBER.** Enter all task numbers as they appear in the report, e.g. 05; RF0330201; T4112.
- 5f. WORK UNIT NUMBER.** Enter all work unit numbers as they appear in the report, e.g. 001; AFAPL30480105.
- 6. AUTHOR(S).** Enter name(s) of person(s) responsible for writing the report, performing the research, or credited with the content of the report. The form of entry is the last name, first name, middle initial, and additional qualifiers separated by commas, e.g. Smith, Richard, J, Jr.
- 7. PERFORMING ORGANIZATION NAME(S) AND ADDRESS(ES).** Self-explanatory.
- 8. PERFORMING ORGANIZATION REPORT NUMBER.** Enter all unique alphanumeric report numbers assigned by the performing organization, e.g. BRL-1234; AFWL-TR-85-4017-Vol-21-PT-2.
- 9. SPONSORING/MONITORING AGENCY NAME(S) AND ADDRESS(ES).** Enter the name and address of the organization(s) financially responsible for and monitoring the work.
- 10. SPONSOR/MONITOR'S ACRONYM(S).** Enter, if available, e.g. BRL, ARDEC, NADC.
- 11. SPONSOR/MONITOR'S REPORT NUMBER(S).** Enter report number as assigned by the sponsoring/monitoring agency, if available, e.g. BRL-TR-829; -215.
- 12. DISTRIBUTION/AVAILABILITY STATEMENT.** Use agency-mandated availability statements to indicate the public availability or distribution limitations of the report. If additional limitations/ restrictions or special markings are indicated, follow agency authorization procedures, e.g. RD/FRD, PROPIN, ITAR, etc. Include copyright information.
- 13. SUPPLEMENTARY NOTES.** Enter information not included elsewhere such as: prepared in cooperation with; translation of; report supersedes; old edition number, etc.
- 14. ABSTRACT.** A brief (approximately 200 words) factual summary of the most significant information.
- 15. SUBJECT TERMS.** Key words or phrases identifying major concepts in the report.
- 16. SECURITY CLASSIFICATION.** Enter security classification in accordance with security classification regulations, e.g. U, C, S, etc. If this form contains classified information, stamp classification level on the top and bottom of this page.
- 17. LIMITATION OF ABSTRACT.** This block must be completed to assign a distribution limitation to the abstract. Enter UU (Unclassified Unlimited) or SAR (Same as Report). An entry in this block is necessary if the abstract is to be limited.

Final Report

**Airborne Aero-Optical Laboratory - Transonic
FA9550-13-1-0001**

**Eric J. Jumper
Professor, University of Notre Dame
Department of Aerospace and Mechanical Engineering
University of Notre Dame
Notre Dame, IN 46556**

3 October 3, 2016

Abstract

This report covers the third year of the Airborne Aero-Optics Laboratory-Transonic (AAOL-T) program. Aero-optics severely limits an airborne directed-energy system's lethal field of regard; aero-optics refers to the deleterious effect that the density fluctuations in the flow have on an airborne optical system. The AAOL-T program studies aero-optical aberration problems from experimental, theoretical and computational approaches; the most unique part of the program is that we also perform flight tests using Falcon 10's, capable of testing at greater than Mach 0.8. The program makes use of two aircraft, one to project a small-aperture, diverging beam toward an optical turret on the second, laboratory aircraft. The third year of the program has been productive with thirty-one flights flown in support of both the baseline program and to support AFRL/DARPA 40% ABC Turret testing, of which 5 flights plus seven at the end of September 2014 were under the baseline program. During the baseline program, extensive measurements of aero-optical environment around both hemisphere-on-cylinder and hemisphere-only turrets were performed for Mach range between 0.5 and 0.8. Fluidic environment was also studied in-flight by collecting simultaneous unsteady pressure data over an array of pressure sensors on the surface of these turrets for Mach between 0.5 and 0.8. In addition to collecting the aero-optical data in flight, the baseline data was used in a wide range of analysis of these data and using the data to explore advanced techniques in adaptive optics. The report describes mainly analysis of data and the computational work done in year three of the program.

Airborne Aero-Optics Laboratory-Transonic (AAOL-T) Progress Report

I. INTRODUCTION

This report covers the third year of the Airborne Aero-Optics Laboratory-Transonic (AAOL-T) Program. The partners in the program are Notre Dame, the Air Force Institute of Technology and MZA. Aero-optics severely limits an airborne directed-energy system's lethal field of regard; in its most restrictive definition, aero-optics refers to the deleterious effect that the density fluctuations in the flow over the exit or receiving pupil have on an airborne optical system, thus the name "aero-optics." Except for some wavefront gathering on the AirBorne Laser, ABL, near the end of its program to assess aero-optic scaling laws, the AAOL [1] and present AAOL-T programs are the only programs to collect high-quality, aero-optically-aberrated wavefront data in flight [2,3,4]. Both programs deal with aero effects on the optical beam control systems of airborne optical systems. Because AAOL-T is a continuation of AAOL many of the original objectives of the AAOL program are also part of the objectives of the present AAOL-T program. The AAOL-T program continues to include Aero-Optics as its primary focus but now at higher Mach numbers [5]; however, the new program has additional objectives that were not part of AAOL: these specifically include aero-mechanical studies, more emphasis on mitigation approaches that include adaptive optics, and specific emphasis on support of other programs. In the year-one annual report, we reported on approaches in understanding unsteady pressure data collected on the Cessna Citation version of the AAOL continued from the end of the AAOL program into the AAOL-T program. As will be described below, in our first safety-of-flight campaign using the new (Falcon 10) aircraft we flew the same pressure turret used in the Citation in conjunction with our first safety-of-flight campaign in February 2014. Also, our support of flight tests for the AFRL/DARPA 40% scale ABC turret began in year-two and is continuing as the report is being written.

Like the AAOL program, AAOL-T program makes use of two aircraft, one to project a small-aperture, diverging beam toward an optical turret on the second, laboratory aircraft. The title of the present grant ends with the word "Transonic;" and required that the program migrate from the Cessna Citation Bravos, which were limited to Mach ~0.7, to the Falcon 10 that can cruise above Mach 0.8. By February 2014, all of the modifications of the new Falcon 10 were complete and both baseline aero-optic data and unsteady pressure data have been taken and analyzed; our high-fidelity CFD effort has also continued. As in year two, this year has also been productive in producing journal articles and meeting papers.

The laboratory Falcon 10 is owned by Notre Dame and was donated to the program by Mr. Matthew McDevitt. At least in the near term, a video of the Notre Dame open house for the AAOL-T can be viewed at: <http://news.nd.edu/news/49299-falcon-10-aircraft-donation-enables-research-at-transonic-speeds/>.

II. AAOL-T FLIGHT-TESTS

In a standard data-acquisition flight test, two Falcon 10s fly in formation at a nominal 50 m separation as shown in Figure 1. A diverging small-aperture 0.532 μm laser is directed from the source aircraft to the turret on the laboratory aircraft, diverging to over fill the turret aperture.

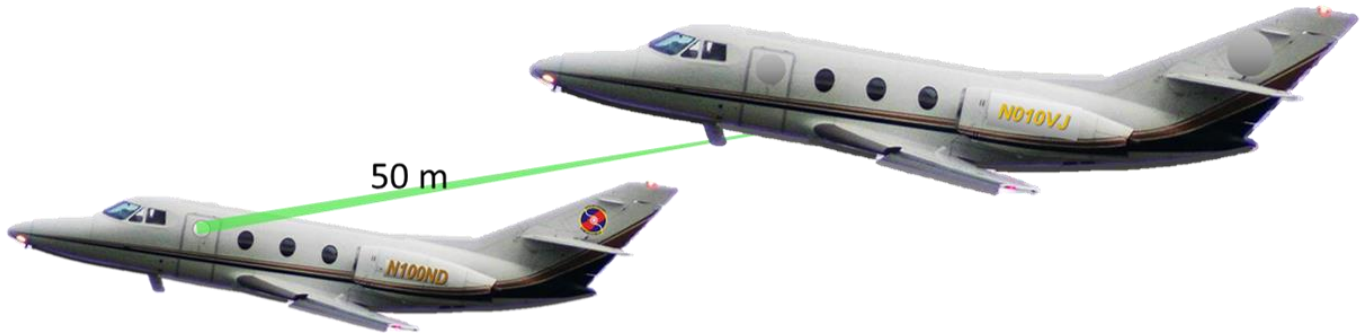


Figure 1. Formation flight with nominal 50 m separation showing diverging source beam emanating from the source aircraft and overfilling turret aperture on laboratory aircraft



Figure 2. View from inside the source aircraft.

The baseline AAOL turret can be configured as either a hemisphere, a hemisphere with a cylindrical base, a spherically-conformal window, a flat window and some geometry changes at the base of the turret. All of these configurations were flown in the previous program at Mach numbers less than Mach 0.7 and these have all been re-flown at Mach Numbers up to Mach 0.8; these were completed in the third year. There is some discussion of the differences in later Sections. In addition, the AAOL-T program supported testing of the Air Force Research Laboratory/DARPA 40% ABC Turret. The flight campaigns are listed in Table 1. As can be seen, only the last three Campaigns were flown in the third year and only one of these was for the baseline program; however, data reduction for the one campaign in year 3 and for the two in the previous year have continued and are now continuing along with planning for the next campaign. It should not be forgotten that the program also includes computational work and testing in wind tunnels. At this writing we are testing mitigation devices and techniques that will be flown in our next campaign. The progress on computational efforts will be covered in a later Section.

TABLE 1

AAOL-T Flight Campaigns

I.	Safety of Flight and Unsteady Pressure <ul style="list-style-type: none"> • 4 Sorties, February 24 - 28, 2014
II.	RVSM Certification Test Flights (Reduced Vertical Separation Minimum) <ul style="list-style-type: none"> • 2 Sorties, March 3 – 6, 2014
III.	Optical Data <ul style="list-style-type: none"> • 5 Sorties, April 16-24, 2014
IV.	ABC 40% Turret <ul style="list-style-type: none"> • 8 Sorties, June 12 – 19
V.	ABC 40% Turret <ul style="list-style-type: none"> • 14 Sorties, August 15 – 25
VI.	Optical Data <ul style="list-style-type: none"> • 7 Sorties, September 16 – 18, 2014
VII.	ABC 40% Turret <ul style="list-style-type: none"> • 12 Sorties, October 8 – 22, 2014
VIII.	Optical Data <ul style="list-style-type: none"> • 5 Sorties, March 23 -27, 2015
IX.	ABC 40% Turret <ul style="list-style-type: none"> • 5 Sorties, April 21 – 24, 2015
X.	ABC 40% Turret <ul style="list-style-type: none"> • 9 Sorties, August 26 – 31, 2015

III. AERO-OPTICAL INVESTIGATION OF TRANSONIC FLOW FEATURES AND SHOCK DYNAMICS ON HEMISPHERE-ON-CYLINDER TURRETS

Flow over turrets is considered to enter the transonic flow regime for Mach numbers greater than 0.55 [6,7]. Above this critical Mach number, flow becomes locally supersonic on the turret. These locally supersonic flow regions can affect the various flow features on the turret. Figure 3 shows the flow features on a turret in the transonic regime. The most notable difference from a turret in subsonic flow is the presence of a local shock on the turret. The exact location and behavior of this shock is dependent on the freestream Mach number [5,8,9]. This shock also can induce separation downstream of it, either causing premature wake formation or locally introducing additional optically-aberrating turbulence. Other than the presence of the shock, many subsonic flow features around the turret are still present in the transonic regime. A necklace vortex forms as the boundary layer rolls up near the base of the turret and extends downstream. Whether induced by the shock or the adverse pressure gradient on the downstream portion of the turret, separation occurs and forms a fully turbulent wake. The upstream portion of the turret exhibits little turbulence, as the accelerating flow remains attached and boundary layer is thin.

It is difficult to study realistic-size turrets at high transonic speeds in tunnels, as it requires specially-designed and expensive to run tunnels with porous walls to eliminate tunnel blockage effects. Furthermore, to perform aero-optical measurements in large tunnels is not a simple task. Our wind tunnel at Notre Dame has been modified to increase its Mach number; however, with a turret in it we have only been able to get it to approximately Mach 0.6. This is why the AAOL and AAOL-T programs were designed to study aero-optical environment in flight [10], using first

Cessna Citations and in the AAOL-T program Falcon 10 planes, capable of flying up to $M = 0.85$, to specifically study transonic effects in flight.

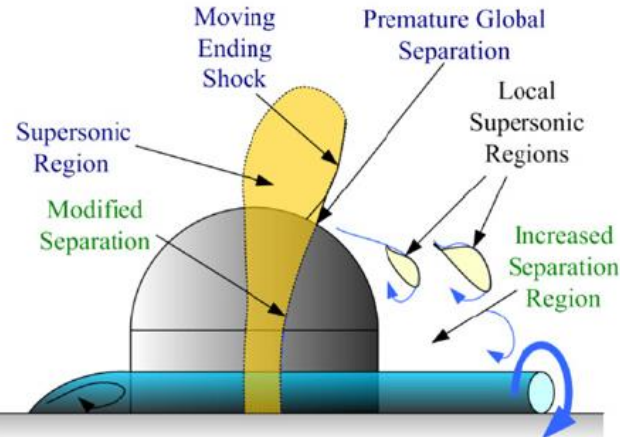


Figure 3. Transonic flow features on the turret. From [6].

The following subsections present results of recent aero-optical flight measurements made over years two and three of the program using the baseline AAOL turret with different aperture/window geometries over a wide range of elevation and azimuthal angles for a range of Mach numbers between 0.5 and 0.8.

Experimental Setup. Wavefront measurements were performed on the AAOL-T [10]. The baseline AAOL turret is 1ft. in diameter with a 4 in. The turret assembly features a fast steering mirror (FSM) to stabilize the beam on the optical bench. Pictures of the turret and optical bench are shown in Figure 4 and Figure 5 shows a schematic of the optical setup in the laboratory aircraft.



Figure 4. The AAOL turret installed on AAOL-T, left and the instrumented optical bench, right.

Two separate flight campaigns, Campaigns VI and VIII (see TABLE 1) were conducted to investigate aero-optics of the turret with different window geometries. During the first campaign, the optical environment around the flat-window turret was investigated at the following

Mach/altitudes: 0.5/15,000 ft, 0.6/18,000 ft, 0.7/26,000 ft and 0.8/26,000 ft. During this campaign, wavefront measurements were performed using a high-speed Shack-Hartmann wavefront sensor. Similar to the data collection during AAOL program, two different acquisition modes were used for wavefronts: slewing maneuvers and fixed data. Slewing maneuvers involved the laser aircraft moving relative to the laboratory aircraft while wavefronts were continuously acquired; these maneuvers allow for rapid mapping of the optical environment around the turret [2,3]. Fixed data involved the laser plane maintaining a fixed position with respect to the laboratory aircraft. These acquisitions were performed at a higher sampling rate, as the goal of fixed data acquisitions is to investigate specific flow phenomena with a better temporal resolution. Wavefronts were collected with the spatial resolution of 32x32 subapertures and sample rates of 25 kHz for 0.7 seconds for fixed points and 3 kHz for 10-30 seconds for slewing maneuvers. Simultaneous with the 2D wavefronts, the overall beam jitter was also measured using a position sensing device. The jitter was acquired along with the turret azimuthal/elevation angle and FSM position information at 25 kHz for 10s. Flight conditions were also recorded with the wavefront and jitter measurements. The aircraft separation was measured using a differential GPS system.

During the second campaign, the turret with both the flat- and the conformal windows was flown at the following Mach/altitudes: 0.5/15,000 ft, 0.6/15,000 ft, 0.6/16,000 ft, 0.7/32,000 ft, 0.7/35,000 ft, 0.7/32,000 ft and 0.8/35,000 ft and optical data at both fixed points and slewing maneuvers were collected. During this campaign, wavefronts were collected with the better spatial resolution of 40x40 subapertures and higher sample rates of 30 kHz for fixed points and 2 kHz for slewing maneuvers. Simultaneous with the 2D wavefronts, the beam jitter was also measured using a position sensing device at 50 kHz for 30 seconds.

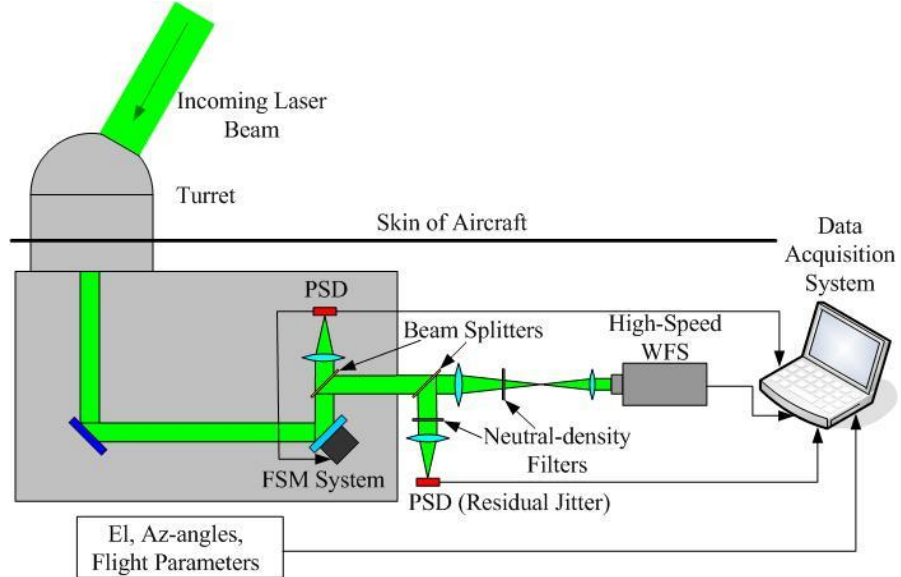


Figure 5. Schematic of the optical setup.

Data Analysis. Reducing the Shack-Hartmann images gives the measured wavefronts, W , as a function of location on the aperture and time, $W = W(x, y, t)$. Through least-squares plane fitting, any residual tip/tilt is removed from the wavefronts, and the steady lensing is removed by removing the mean of the wavefront at every subaperture. The optical path difference (OPD) is the conjugate of the wavefront, $OPD(x, y, t) = -W(x, y, t)$. To determine the variation of the OPD across the aperture, the spatial RMS is computed at every time step, $OPD_{RMS}(t) = \sqrt{\langle OPD(x, y, t)^2 \rangle_{(x, y)}}$. For

some aperture angles and Mach numbers, a spatial distribution of the time-averaged OPD_{RMS} at every point over the aperture, $OPD_{RMS}(x,y)$, was computed as, $OPD_{RMS}(x,y) = \sqrt{OPD(x,y,t)^2}$. The time-average OPD_{RMS} , quantifies average amount of aberration present in the beam for a specific viewing direction. Similar to subsonic aero-optical studies, [2,3], the OPD_{RMS} is normalized by the flight conditions, $OPD_{RMS,Norm} = OPD_{RMS} / \left(\frac{\rho}{\rho_{SL}} M^2 D \right)$ to compare the aero-optical performance of the turret across various Mach numbers. In this normalization, ρ is the freestream density, ρ_{SL} is the density at sea level, M is the Mach number and D is the turret diameter. This scaling has been previously shown to collapse subsonic data acquired in flight and in the tunnel [2].

The turret azimuthal (Az) and elevation (El) angles were recast into a coordinate system that is more useful from a fluid dynamics perspective. This system uses a viewing angle, α , that determines how far downstream the turret is looking and the modified elevation angle, β , that quantifies how far the turret is looking away from the wall of the aircraft. The viewing angle is given by $\alpha = \cos^{-1}(\cos(Az)\cos(El))$, and the modified elevation angle is given by $\beta = \tan^{-1}\left(\frac{\tan(El)}{\sin(Az)}\right)$,

as shown in Figure 6.

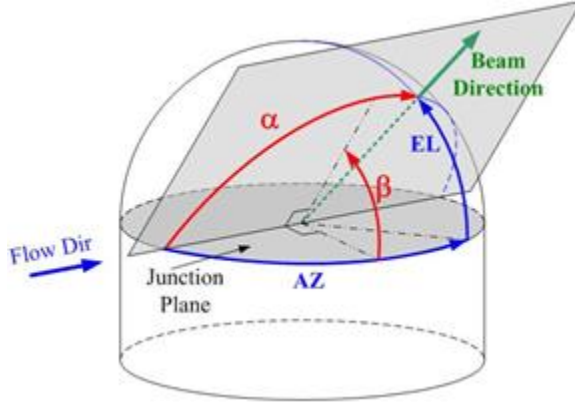


Figure 6. Definitions of azimuthal (Az) and elevation (El) angles to viewing angle (α) and modified elevation angle (β). From [2].

Results Flat-Window Turret. Figure 7 shows the normalized OPD_{RMS} values for the flat-window turret as a function of Mach number and viewing angle. As $M = 0.5$ was extensively studied during AAOL program, so only four points for $M = 0.5$ were collected, mainly for comparison and repeatability purposes. For $M = 0.6$, OPD_{RMS} values are fairly small for $\alpha < 90^\circ$, as the flow is attached over the flat-window aperture; OPD_{RMS} values are very similar to $M = 0.5$ values, see [2]. Also, in [2] it was shown that at subsonic speeds over a range of viewing angles between 90° and 100° , a local separation bubble forms over the flat aperture, causing a local increase in OPD_{RMS} values. At $M = 0.6$ the local shock on top of the turret is very weak to modify the otherwise subsonic flow over the turret, so a rather similar peak in OPD_{RMS} is present at $M = 0.6$; the peak location is slightly shifted toward 90° . At $\alpha = 110^\circ$ the flow separates, and for large viewing angles $\alpha > 110^\circ$ OPD_{RMS} continuously increase due to looking through the separated wake of the turret. Again, this behavior is very similar to OPD_{RMS} results at $M = 0.5$.

For a higher $M = 0.7$, the location of the local peak due to the separation bubble is around 90° and approximately unchanged from $M = 0.6$. The unsteady local peak is sharper, compared to $M=0.6$ case; inspection of wavefronts have revealed the presence of the shock approximately in the

middle of the aperture. The flow separates around 110° as well, but the wake appears to be more optically-aberrating.

For $M = 0.8$, a stronger shock was found to be present over the flat aperture between viewing angles 75° and 90° , so the overall levels of OPD_{RMS} are significantly higher, compared to values at the same angle range at lower Mach numbers. The shock was found to be unsteady and moving approximately in the middle of the aperture, see spatial distributions of OPD_{RMS} for shock-induced wavefronts in Figure 8. The flow separation is also affected by the shock presence and appears to occur slightly upstream, at $\alpha = 105^\circ$, compared to $M = 0.6$ and $M = 0.7$. There is no local peak that is indicative of a separation bubble for $M = 0.8$, indicating that the shock-induced separation over the flat-window prevents its formation.

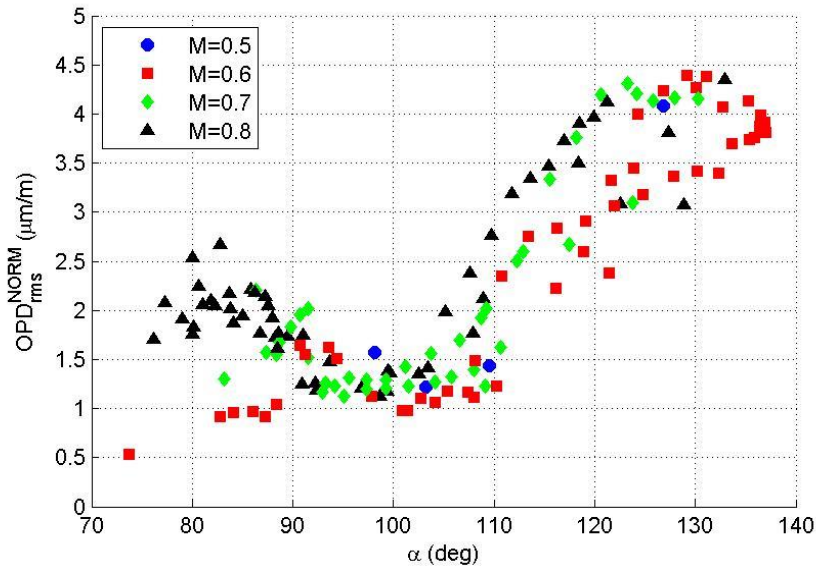


Figure 7. Normalized OPD_{RMS} versus viewing angle for $M = 0.5-0.8$ for the flat-window turret.

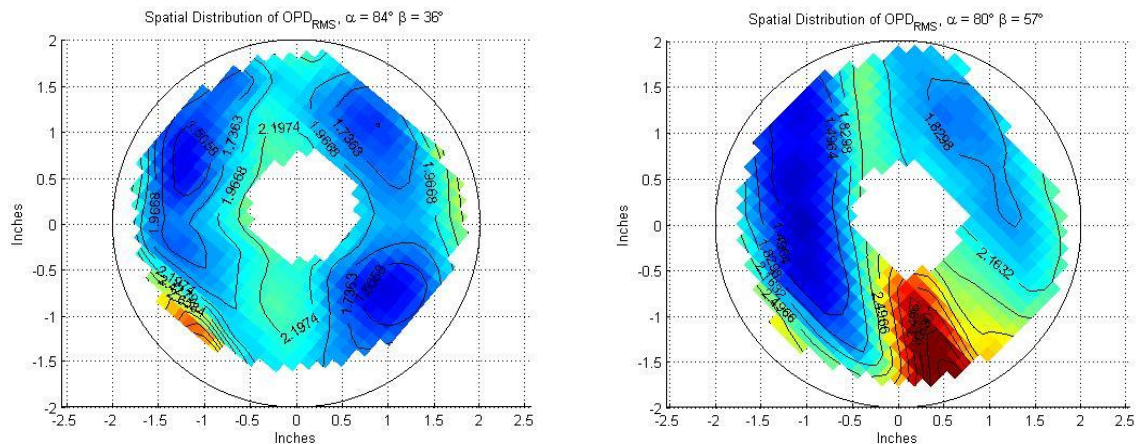


Figure 8. Spatial Distributions of OPD_{RMS} for the flat-window aperture. Left: $Az = 82^\circ$ and $El = 36^\circ$ ($\alpha=84^\circ$) $M = 0.7$. Right: $Az = 72^\circ$ and $El = 56^\circ$ ($\alpha=80^\circ$) $M = 0.8$. Flow goes from left to right.

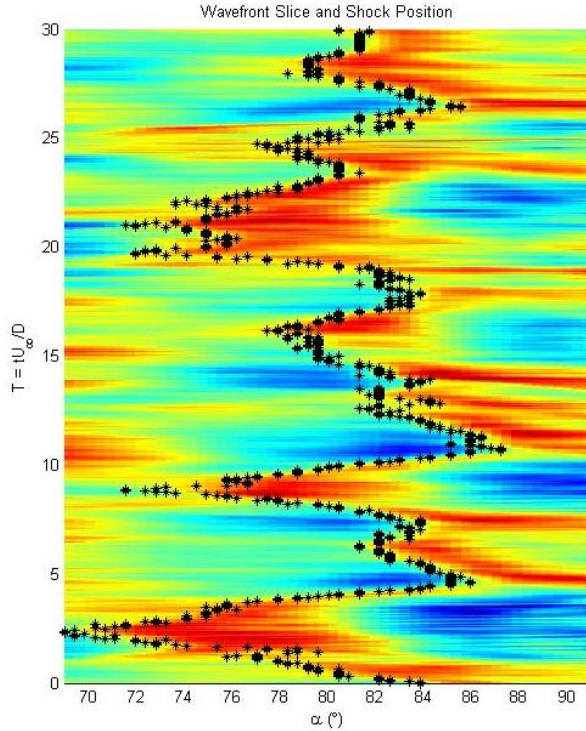


Figure 9: Spatial-temporal evolution of 1-D slice of wavefront for $M = 0.8$ for aperture located at $\alpha = 80^\circ$, $\beta = 43^\circ$. Black circles indicate the approximate shock location.

The normalized spatial distributions of OPD_{RMS} are shown in Figure 8. Both the $M = 0.7$ wavefronts, left and $M = 0.8$ wavefronts, right show an increase in OPD_{RMS} in a narrow band near the center of the aperture due to the presence of the unsteady shock. This is the shock location for both cases. Because the shock location is near the center of the aperture, even though the viewing angle and Mach number are slightly different between the two cases, it is believed that the flat window has an “anchoring” effect on the shock in that it forces it to the center of the aperture, on average. One possible reason for this “anchoring” effect is that the separation bubble forms a fluidic curved surface over the aperture. The topology of the separation bubble is very sensitive to the flat-window position, as well as the flow environment. For $M = 0.7$ the shock is formed over the curved fluidic surface, but the shock is fairly weak to modify it. The shock becomes much stronger at $M = 0.8$, essentially destroying the bubble. As it will be shown later in this paper in Figure 10, the resulted OPD_{RMS} for both the flat- and the conformal-window aperture are very similar at $M = 0.8$, confirming that the aperture geometry becomes a secondary factor, compared to the shock-induced effects.

Figure 9 shows a one-dimensional slice of wavefronts taken at $M = 0.8$ for the aperture located at $\alpha = 82^\circ$ and $\beta = 43^\circ$. The shock location was captured in α - β coordinates for given fixed β . The discontinuity of a shock causes a sharp change in the wavefront, so shock tracking was done by stepping along α at the β of interest to find the location of maximum slope in the OPD_{RMS} ; a similar analysis was performed to study the shock dynamics on a 2D turret in the wind tunnel in [4,5]. The black filled circles show the location of maximum positive wavefront slope, which is presumed to be related to the instantaneous shock position. This maximum slope corresponds to the location of the shock. The shock moves between a relatively wide range of $\alpha = 70^\circ$ and 88° ; this unsteady shock motion is as a cause of the increase in OPD_{RMS} observed in the $M = 0.8$ data from Figure 5. The shock movement, although oscillatory, doesn’t appear to be periodic in nature and the shock does not “wander” off of the aperture.

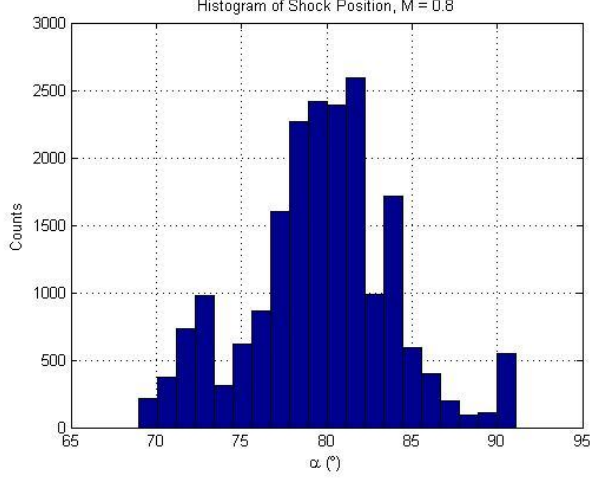


Figure 10: Histogram of the shock position for $M = 0.8$ at $Az = 72^\circ$, $El = 56^\circ$.

The histogram of the shock position for $M = 0.8$ is shown in Figure 10. The shock is between 71° and 87° 90% of the time, and the average location is at 80° . For $M = 0.7$ (not shown), the shock moves approximately the same amount as for $M = 0.8$.

The spectra of the shock position for both $M = 0.7$ and $M = 0.8$ are shown in Figure 11. There isn't much discernable difference between the frequency content of the shock movement for the two Mach numbers. Both exhibit a peak near $St = 0.15$ and fall off after that. This peak has been associated with the movement of the separation line on a hemisphere on cylinder turret for subsonic [11] and transonic [12] flow regimes. As the separation bubble is sensitive to the global environment, which is primarily governed by the separated region downstream of the turret, this single peak in the shock spectra indicates that the shock dynamics is linked to the separation line dynamics.

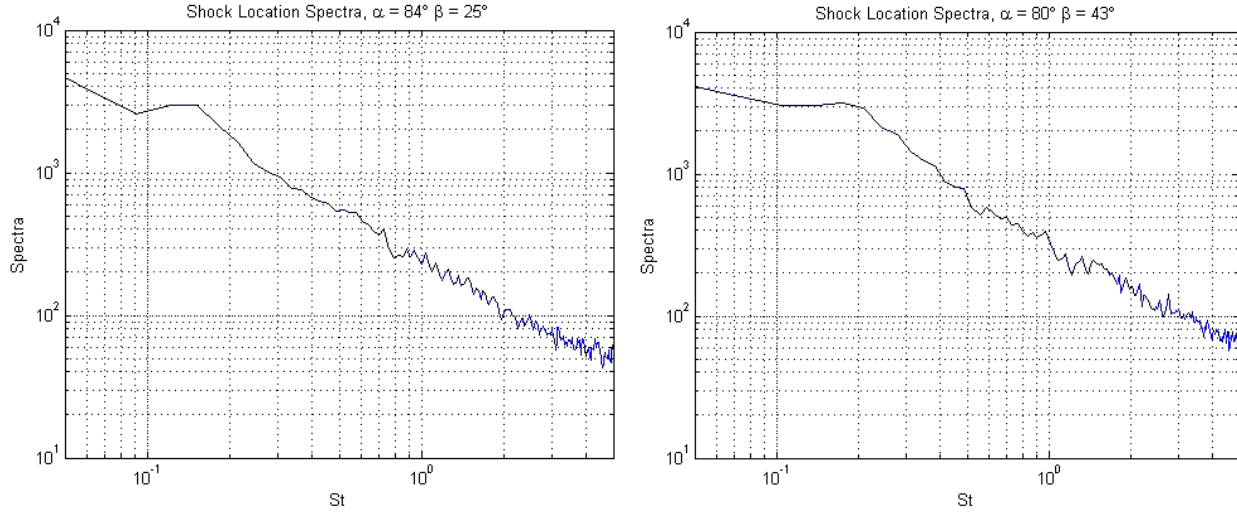


Figure 11: Shock location spectra for $M = 0.7$, left and $M = 0.8$, right.

Results Conformal-Window Turret. Figure 12 shows the normalized OPD_{RMS} values for the conformal-window turret as a function of Mach number and viewing angle. At subsonic Mach numbers of 0.5 and 0.6, the flow is subsonic everywhere around the turret. Unlike for the flat-window turret, shown in Figure 5, the flow stays attached over the aperture for side-looking angles 80-90 degrees with the low resulting OPD_{RMS} , as the conformal-window does not trip the flow around the aperture. For higher Mach numbers of 0.7 and 0.8 the unsteady shock appears over the

aperture at the viewing angle of approximately 80 degrees, resulting in a local increase of OPD_{RMS} . Optical distortions at looking-back angles, $\alpha > 100$ degrees, are due to the wake downstream of the turret and are similar for both the flat- and conformal-window turrets, see Figure 7 for comparison.

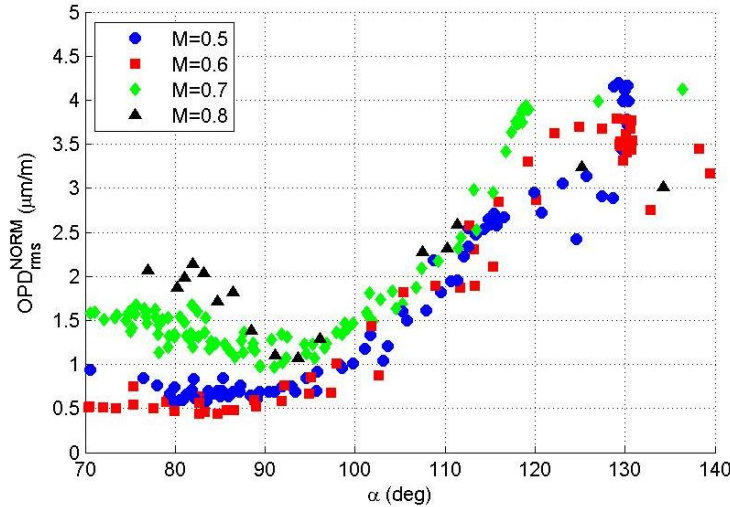


Figure 12. Normalized OPD_{RMS} versus viewing angle for $M = 0.5-0.8$ for the conformal-window turret.

To visualize the shock location on the turret, spatial distribution of OPD_{RMS} over the aperture at side-looking angles were projected on the turret. The shock creates additional localized distortions and it is visible as a line of the increased distortions, as shown in Figure 13. The average shock location is around $\alpha = 80$ degrees and fairly independent of the modified elevation angle. The streamwise shock extent increases with the Mach number increase.

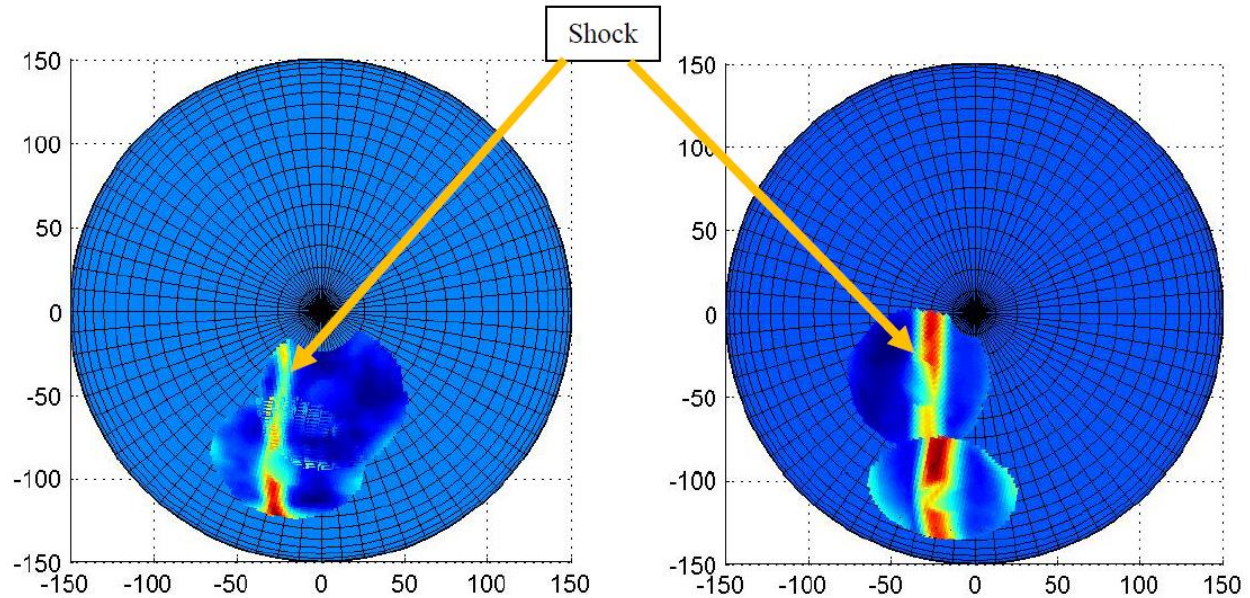


Figure 13. The top view of spatial variation of wavefronts for side-looking angles, indicating the shock location for $M=0.7$ (left) and $M=0.8$ (right). Flow goes from left to right.

To further study the temporal shock dynamics, spatial-temporal evolution 1-D slices of the wavefronts were extracted at different β -locations and Mach numbers and the instantaneous shock location was extracted, as it was described before. Figure 14 shows temporal evolution of a one-

dimensional slice of the wavefront for a conformal window turret taken at $M = 0.7$ and $M = 0.8$ with $\beta = 60^\circ$ and $\beta = 50^\circ$, respectively. The black dots represent the shock location for each time step. The shock motion is not periodic for either case, although the shock for $M = 0.8$ clearly has a single preferred frequency. Shocks are present consistently for each Mach number. The shock location for $M = 0.7$ varies from 74° to 83° , while for $M = 0.8$ it has a larger range of 70° to 84° . The $M = 0.8$ case also has a larger non-dimensional time between peaks than the $M = 0.7$ case, indicating a lower oscillation frequency content.

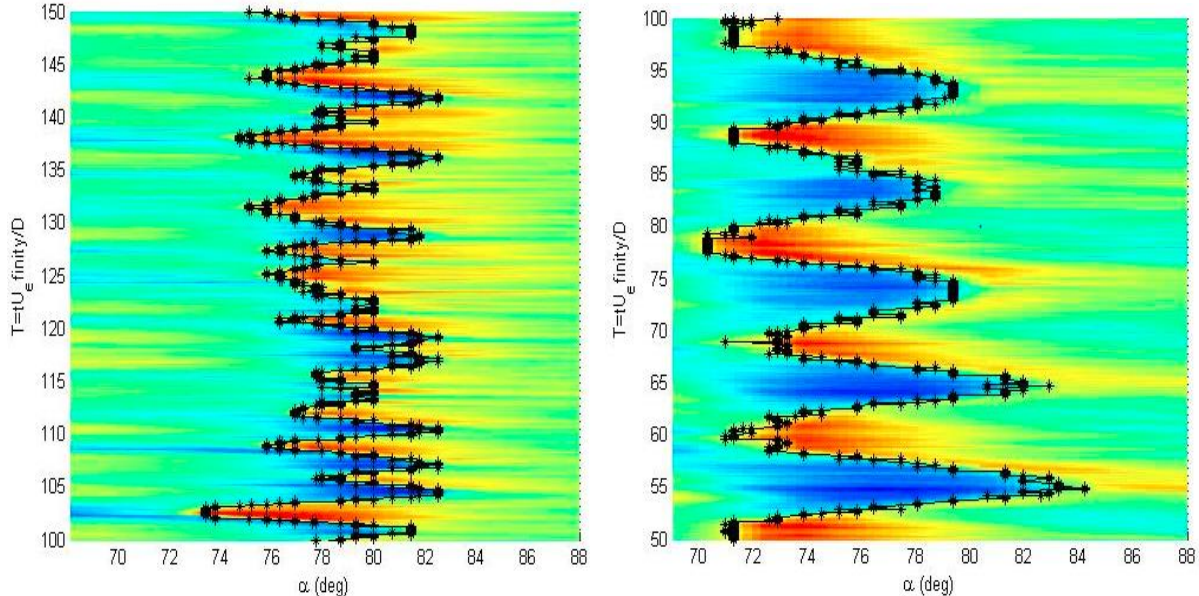


Figure 14: Spatial-temporal evolution of 1-D slice of wavefront data with $M = 0.7$ (left) at $\beta = 60^\circ$ and $M = 0.8$ (right) at $\beta = 50^\circ$. Black circles indicate the approximate shock location.

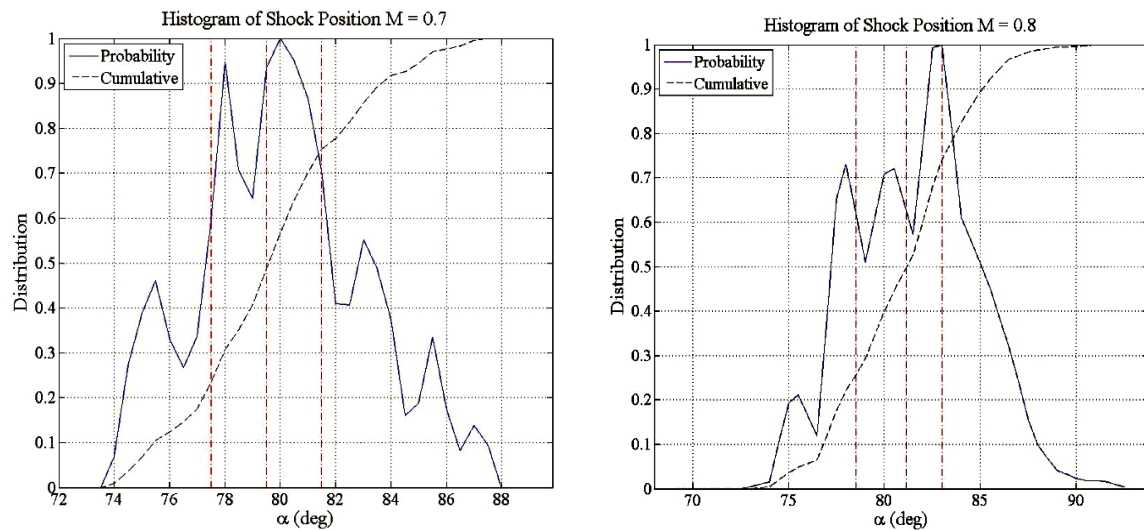


Figure 15: Probability and Cumulative Distribution Functions of shock locations at $\beta = 70^\circ$

Figure 15 shows the probability and cumulative distributions of the shock angles for $M = 0.7$ and $M = 0.8$ at the same β location. In both cases the probability function is not symmetric. The shock location ranges from 74° to 88° at $M = 0.7$, while in the $M = 0.8$ case it has a larger range of 70° to 92° . Figure 16 depicts the median shock locations at different β -angles with bars representing the range of α where the shock is present 90%. The median shock location angle does not change

significantly with changing β for either Mach number, which is consistent with the spatial distribution of OPD_{RMS} in Figure 13. For $M = 0.8$ the shock tends to have a larger range than for $M = 0.7$.

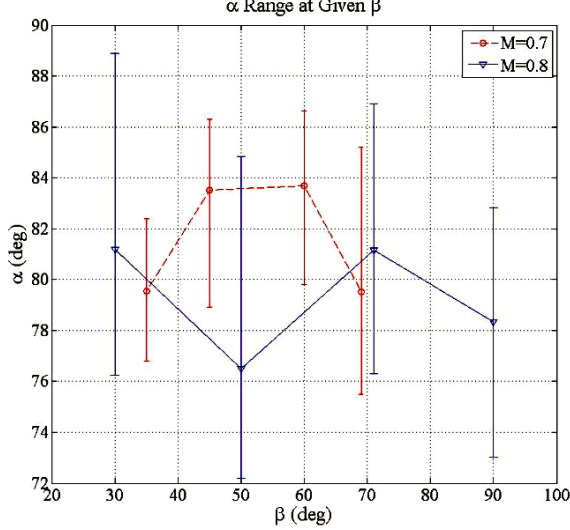


Figure 16: Shock median locations and 90%-range for $M = 0.7$ and $M = 0.8$ for conformal-window turret.

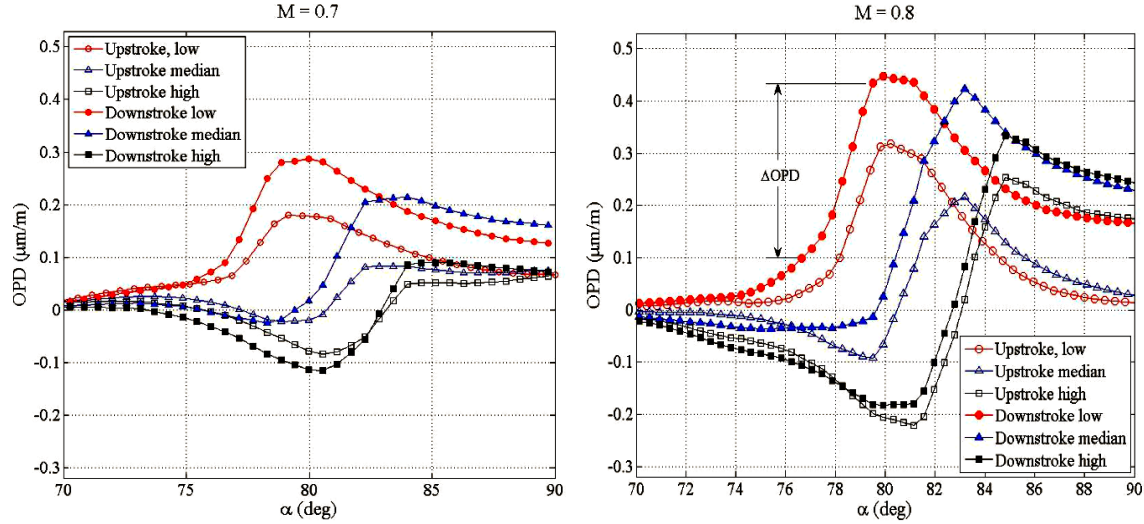


Figure 17: Averaged One-dimensional wavefronts for shock incidences at viewing angles and $\beta = 70^\circ$.

Figure 17 shows one-dimensional mean wavefronts located at the viewing angles corresponding to the locations marked by red dotted lines in Figure 15. At these α -locations the cumulative probability reaches 25% (upstream of the median), 50% (median) and 75% (downstream of the median). These points were selected to represent the wavefront shape and shock dynamics at various moments of the shock motion for each Mach number. They were found by conditionally-averaging all of the instantaneous wavefronts with shocks located at the corresponding viewing angle. The analysis was done separately for time steps where the shock was moving toward higher α (downstroke), and toward lower α (upstroke). The shock optical strength at a given angle was determined by finding the change in OPD across the sharp gradient region in the one-dimensional wavefront, as shown in Figure 17, right. Bounds of the shock were considered to be where the OPD slope was 70% of the maximum slope of the wavefront. The shock strength is consistently greater at

$M = 0.8$, and during the upstroke motion the shock was found to be stronger than during the downstroke motion at each Mach number. The change in OPD is almost constant at $M = 0.7$ with varying viewing angle, while at $M = 0.8$, there is a larger jump in OPD at higher angles.

To illustrate this effect, Figure 18 depicts the average shock strength for both the upstroke and the downstroke motion for different α at $M = 0.7$ and 0.8 . The range of α contains 90% of the data. For $M = 0.7$ the shock strength is almost constant over the range of the viewing angles, but for $M = 0.8$ the shock strength increases as α increases. The upstroke shock strength is consistently higher than the downstroke for both cases. A similar shock behavior was seen in AAOL at $M = 0.65$ [3] and around cylindrical turrets [5], where the shock during the upstroke motion was also found to be stronger, compared to the downstroke motion. In [3] it was proposed that the stronger upstroke shock strength is linked to fluctuations in the separation bubble size. Presented results seem to support this proposition.

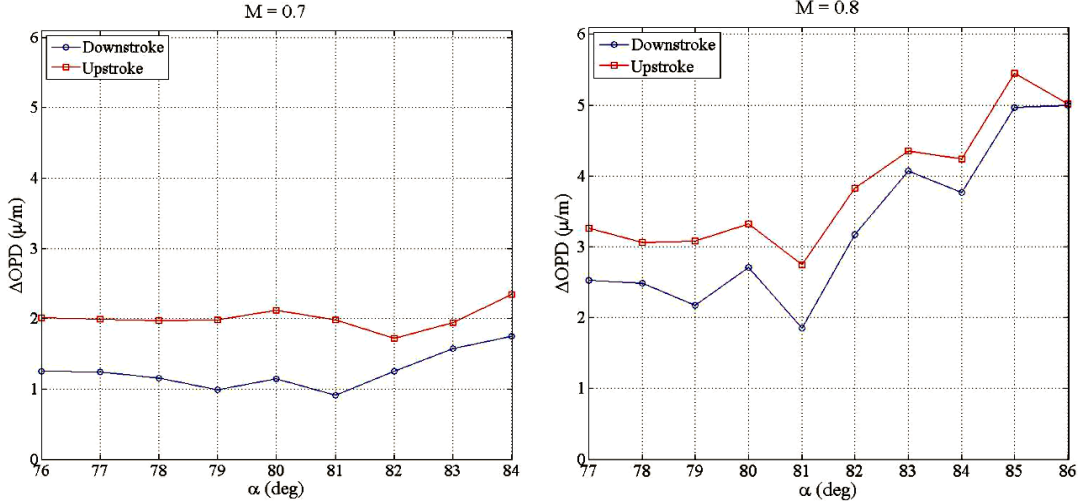


Figure 18: Average Shock Strength Determined Change in OPD Across the Shock at $\beta = 70^\circ$ and $M = 0.8$

The temporal spectra of the shock position for a conformal window at $M = 0.7$ and $M = 0.8$ are shown in Figure 19. The most discernable difference between the two is that the $M = 0.7$ case has peaks around $St = 0.18$ and $St = 0.3$, while the $M = 0.8$ case has only one peak near $St = 0.15$; this lower-frequency dynamics was already observed in Figure 14.

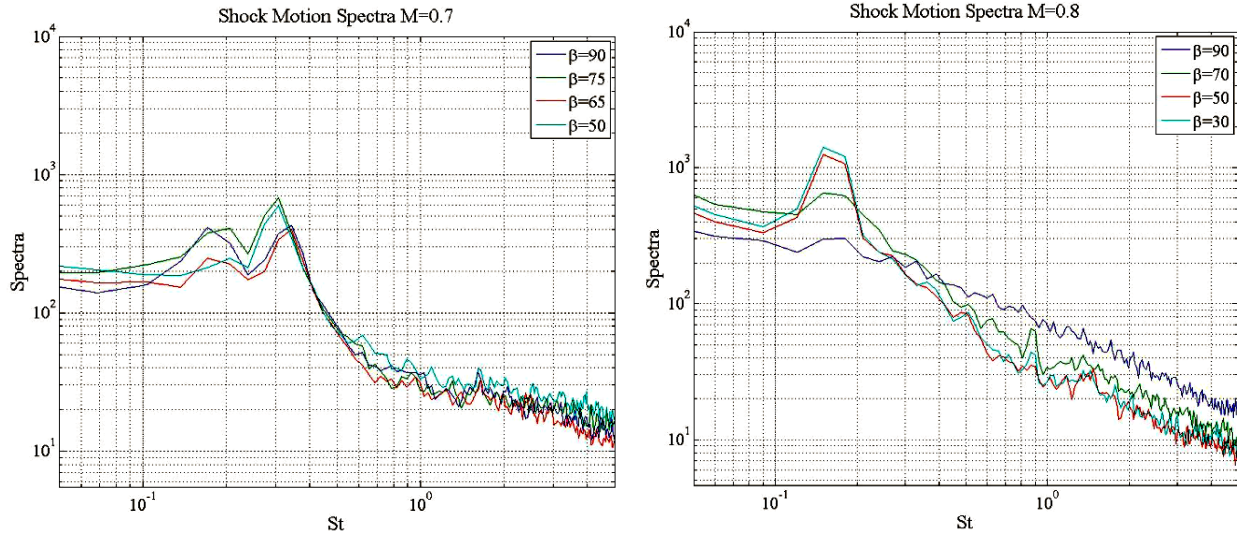


Figure 19: Conformal-Window shock location spectra for $M = 0.7$, left and $M = 0.8$, right.

Results from pressure measurements on AAOL turret [12] have showed similar peak locations for both $M = 0.7$ and 0.8 . To understand a possible mechanism of this low-frequency dynamics, let us recall that a weaker, intermittent shock was observed on the AAOL at a lower $M = 0.65$ [3] with a typical frequency of $St \sim 0.5$. Also, $St = 0.15$ has been associated with the unsteady separation line motion over a wide range of subsonic [11] and transonic [12] Mach numbers. So, while at low transonic speeds the shock dynamics is mostly independent of the separation region dynamics, at higher Mach number the shock becomes strong enough to force a premature separation, effectively coupling or locking-in the shock and the separation line dynamics. In [5] this strong coupling between the shock location and its strength with the location and the size of the separated region was studied over cylindrical turrets and an acoustical feedback was proposed as a possible mechanism for locking the dynamics of the shock and the shock-induced separation region.

Wavefront Spectra in the Wake. To investigate the possible effects of the shock, formed on the turret, on the optical performance of the separated wake, aperture-averaged normalized wavefront spectra were computed for the viewing angle of $\alpha = 120$ degrees for different Mach numbers and window geometries and the results for the flat-window turret are shown in Figure 20, left, and for the conformal-window turret in Figure 20, right. For high viewing angles, the beam traverses through the separated region, dominated by the shear-layer structures. Spectra for all Mach numbers, including transonic ones, show a very good collapse for both window geometries. The peak in spectra is around $St_D = 1.3$, which corresponds to a typical normalized frequency for the shear layer structures at subsonic speeds at these viewing angles [20]. The spectra collapse indicates that once the flow is separated, the presence of the shock does not significantly affect the structures in the separation region. Nevertheless, note that for the highest measured $M = 0.8$, the small secondary, separation-line-related peak appears around $St_D = 0.15$ for both window geometries; this is also consistent with the lock-in mechanism between the shock and the separation region, discussed above.

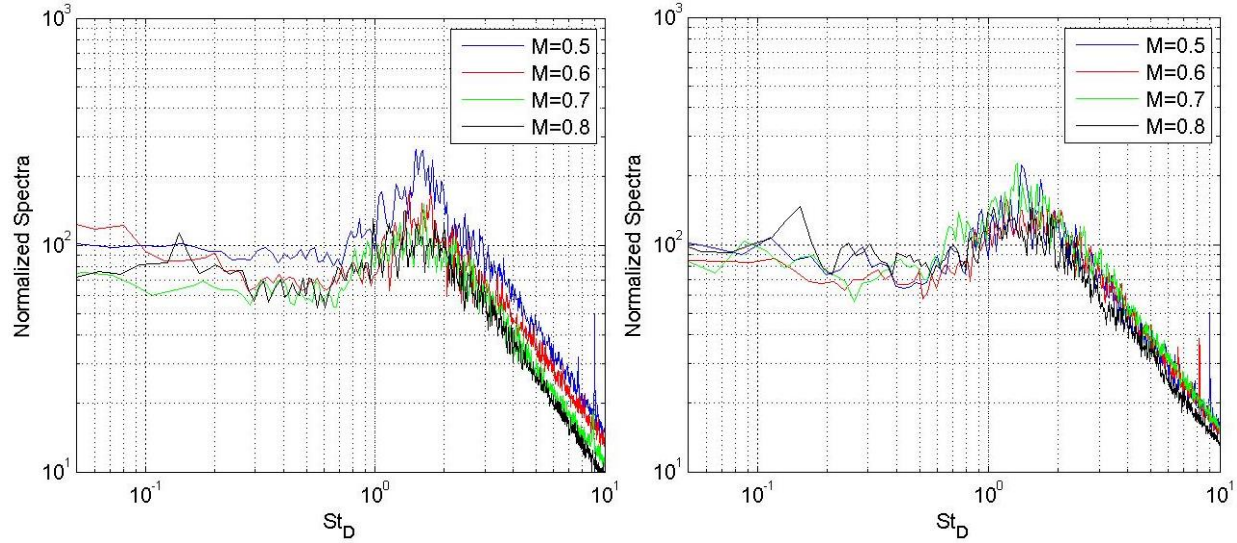


Figure 20. Normalized aperture-averaged wavefront spectra for several Mach numbers for $\alpha = 120$ degrees for the flat-window (left) and the conformal-window (right) turrets.

IV. TRANSONIC FLOW DYNAMICS OVER A HEMISPHERE IN FLIGHT

There are many applications for optical turrets operating on airborne platforms at transonic speeds [6]. However, the optical distortions associated with the flow features around a turret such as an unsteady shock and flow separation, reduce the beam quality [6]. In order to reduce or eliminate optical aberrations it is necessary to better understand the transonic flow features over a hemispherical turret.

Aero-optical effects in the fully subsonic regime have been thoroughly studied and are well understood [1,2,3,6,14,15,16], but at Mach numbers above 0.55 the flow becomes locally supersonic near the top of the turret, resulting in an unsteady local shock earlier shock-induced flow separation [5,6]. The presence of the shock and early separation point not only increase the amount of optical distortion as discussed in the earlier Section, but it also give rise to unsteady pressure disturbances that find their way into the beam train and induce aero-induced jitter.

Pressure and optical measurements have previously been performed on hemisphere-on-cylinder turrets in flight [1,14]. In the AAOL-T program and, we measured unsteady pressure on the baseline AAOL turret in higher, transonic speeds and in particular over the turret configured as a hemisphere-only turret. Both numerical simulations [17,18] and wind tunnel experiments [16] have been performed with hemispheres to better understand the shock and boundary layer effects on optics. In this Section the study is extended to flight testing.

The interaction between the shocks and the separated wake region over bodies with large spanwise curvature is not yet fully understood [9-11]. Measuring the pressure field over the hemisphere surface gives insight into the shock and boundary layer motion from a non-optical point of view. Since both the shock and flow separation are detrimental to beam quality [1,2,13,14], it is important to gain a better understanding of the interaction between them. This knowledge will enable adaptive feedback mechanisms and flow control that will mitigate unwanted aero-optical effects [12].

Experimental Setup. Unsteady local pressure measurements [19] were performed in February of 2014 during in-flight safety of flight testing but have only been analyzed in conjunction with optical data during the 3rd year. The 12-inch diameter AAOL baseline turret was configured as a hemisphere-only and mounted on the Falcon 10 aircraft, see Figure 21, left. The turret was mounted on a frame that allowed for rotation to any desired azimuthal angle and featured a worm-gear system that allowed control the of elevation angle, see Figure 22, right. The hemispherical turret was with 19 pressure sensors on it, shown in Figure 22. The pressure sensors were Kulite differential pressure transducers and were placed approximately uniformly over the entire surface of the hemisphere with a cluster of 7 points centered over the aperture as shown in figure 2. Data was collected for 12 different azimuthal angles between 0 to 180 degrees; the elevation of the aperture was fixed at 45 degrees. Data sets were collected at 15,000 feet for Mach numbers of 0.4, 0.5, 0.6, and 28,000 feet for Mach numbers of 0.7, and 0.8, see TABLE 1 for details; the zero azimuthal angle aligned with the incoming freestream flow. The data were collected at a sampling rate of 25 kHz for 20 seconds during each data set.

Corresponding optical measurements were taken on the AAOL-T in March of 2015 with the optical turret recessed into the aircraft, so only the hemispherical portion of if sticking out, see Figure 23, left.

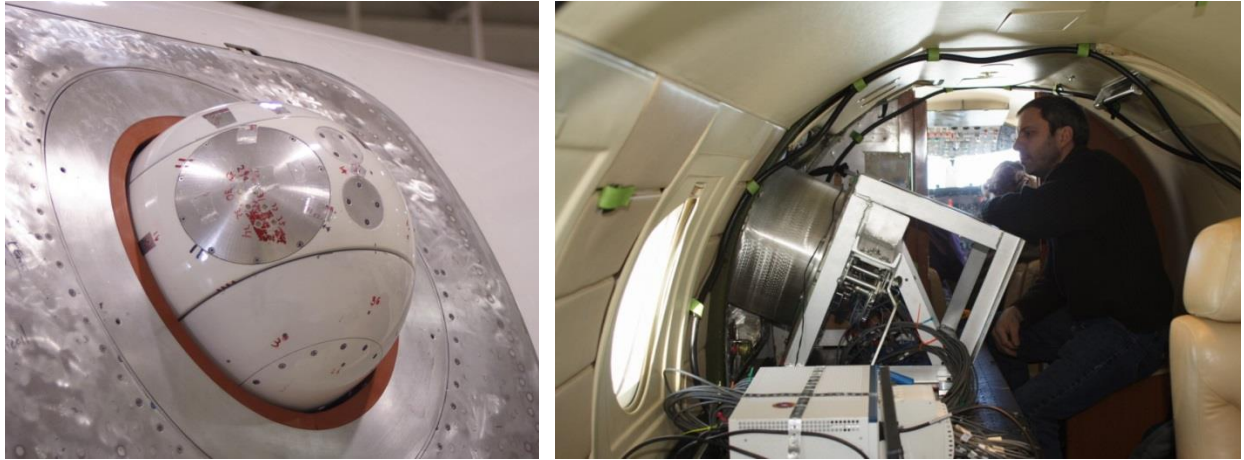


Figure 21: The pressure-instrumented hemispherical turret with the conformal window mounted on the AAOL-T, left and the interior testing bench, right.

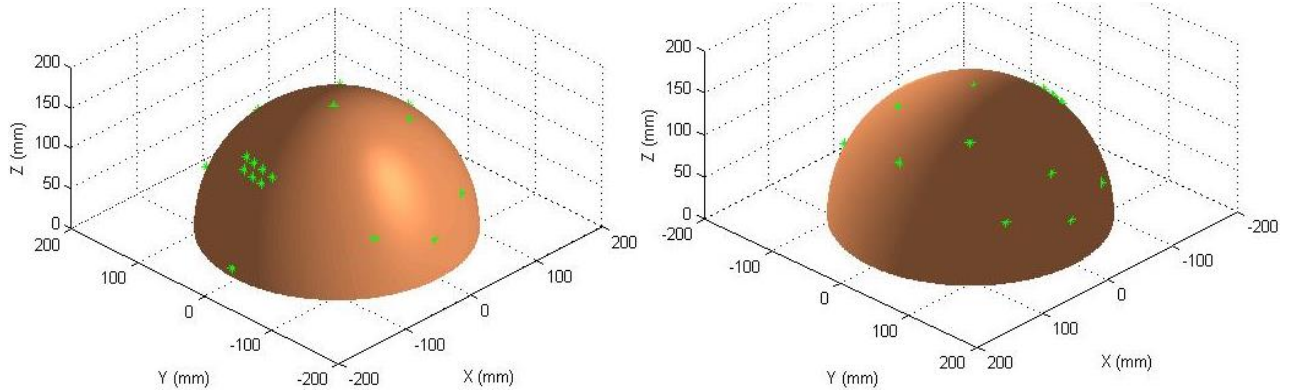


Figure 22. Pressure Port Locations for a single azimuthal angle

TABLE 1
Flight conditions and azimuthal angles for hemispherical turret

Altitude/Mach and Az-anlges (in degrees)
15 kft/0.4: Az = 0 8 20 28 44 90 134 180
15 kft/0.5: Az = 0 8 20 28 44 90 134 180
15 kft/0.6: Az = 0 8 20 28 44 85 88 90 134 180
28 kft/0.7: Az = 0 8 20 28 44 85 88 90 112 134 180
28 kft/0.8: Az = 0 8 20 28 44 85 88 90 97 112 134 180

The optical setup in the laboratory aircraft was described in detail in [20,21] and described in a previous section, see Figure 4, right, for a photo of the optical bench. Figure 21, showing the hemisphere-only turret configuration, can be compared with Figure 4 that shows the baseline AAOL turret in the hemisphere on a cylindrical base configuration. Wavefront measurements were performed using a high-speed Shack-Hartmann wavefront sensor as described in an earlier Section. The wavefront sensor featured 32x32 subapertures at a sample rate of up to 25 kHz. Simultaneous with the 2D wavefronts, the beam jitter was also measured using a position sensing device. The

jitter was acquired with the turret viewing angle and FSM position information at 25 kHz for 10s. Flight conditions were also obtained simultaneous with the wavefront and jitter measurements. The aircraft separation was measured using a differential GPS system.

Two different acquisition modes were used for wavefronts: slewing maneuvers and fixed data. Slewing maneuvers involved the laser aircraft moving relative to the laboratory aircraft while wavefronts were continuously acquired at 3 kHz for at least 15 seconds. These maneuvers allow for rapid mapping of the optical environment around the turret [1,2]. Fixed data involved the laser plane maintaining a fixed position with respect to the laboratory aircraft. These acquisitions were performed at a higher sampling rate of 25 kHz for 0.7 seconds. The goal of fixed data acquisitions is to investigate specific flow phenomenon with a better temporal resolution.



Figure 23: The AAOL turret installed on AAOL-T, left and the instrumented optical bench, right.

Data Analysis. The pressure data from multiple hemisphere orientations were combined to find pressure data over a range of viewing angles. The pressure was normalized by the dynamic pressure to get the pressure coefficient, $C_p = \frac{P - P_{ref}}{\frac{1}{2} \rho U^2}$, where ρ is the freestream density and U is the freestream velocity.

Calculating the root mean square determines the temporal variation of the pressure coefficient at each location, $Cp_{RMS}(t) = \sqrt{Cp(t)^2}$. The pressure spectra were calculated to compare the frequency with both pressure and optical data from other experiments.

The Shack-Hartmann images were reduced using in-house software to obtain the wavefronts, W , as a function of location on the aperture and time, $W = W(\bar{x}, t)$ as described in a previous Section.

Optical results. Figure 24 shows the normalized OPD_{RMS} values as a function of Mach number and viewing angle. As $M = 0.5$ was extensively studied during AAOL program [3], only several points for $M = 0.5$ were collected, mainly for comparison and repeatability purposes. For $M = 0.6$, OPD_{RMS} values are fairly small for $\alpha < 110^\circ$, as the flow is attached over the flat-window aperture; OPD_{RMS} values are very similar to $M = 0.5$ values. At $\alpha = 110^\circ$ the flow separates, so for large viewing angles $\alpha > 110^\circ$ OPD_{RMS} continuously increase due to looking through the separated wake of the turret. Again, this behavior is very similar to OPD_{RMS} results at $M = 0.5$.

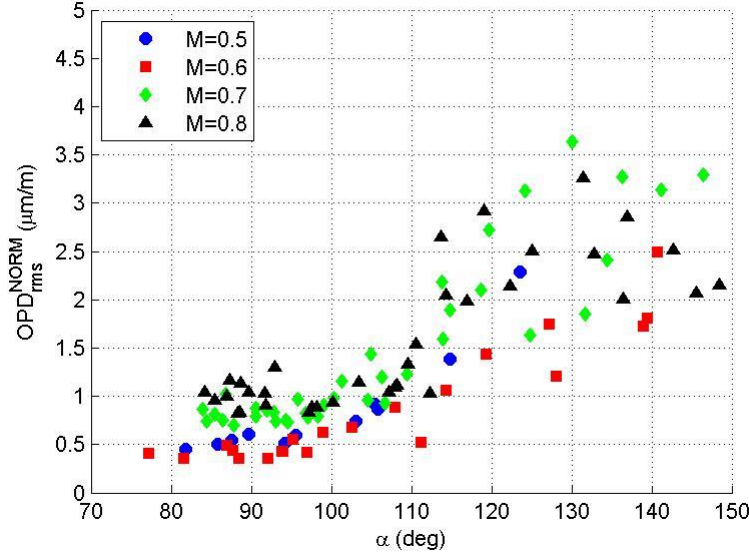


Figure 24: Normalized OPDRMS versus viewing angle for $M = 0.5\text{--}0.8$.

For a higher $M = 0.7$, a small unsteady shock appears near $\alpha = 90$ degrees, thus increasing the local aero-optical distortions near this viewing angle. The flow separates around 110° as well, but the wake arrears to be more optically-aberrating. For $M = 0.8$, the shock intensifies, so the overall levels of OPDRms are higher, compared values at the same angle range at lower Mach numbers. The shock dynamics was found to be similar to the shock dynamics over the hemisphere-on-cylinder turret [20]. Overall, the aero-optical distortions over the hemispherical turret were found to be weaker than for the hemisphere-on-cylinder turret, compare with Figure 12.

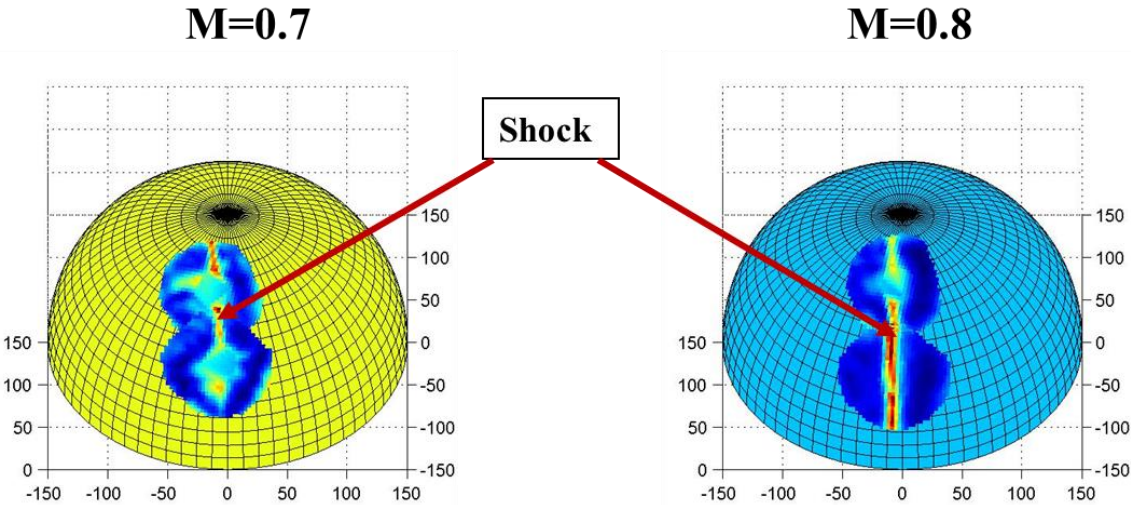


Figure 25. Spatial variations of the wavefronts over the aperture, $Wrms(\alpha,\beta)$, projected on the turret for $M = 0.7$ (left) and $M = 0.8$ (right).

To visualize the shock location on the turret, spatial variations of wavefronts at side-looking angles were projected on the hemispherical turret. Results for $M = 0.7$ and 0.8 are presented in Figure 25. The shock creates additional localized distortions, visible as a line of the increased distortions. The average shock location is around $\alpha = 88$ degrees and fairly independent of the elevation angle, consistent with tunnel tests [23] and numerical simulations [24,25].

Temporal evolution of the wavefronts was used to calculate aperture-averaged wavefront spectra. An example of the spectra for a side-looking angle of $\alpha = 90$ degrees for $M = 0.6, 0.7$ and 0.8 are shown in Figure 26, left. The increase in spectra increase in the frequency range $St_D = 0.1-1$ at $M = 0.7$ and 0.8 due to the shock appearance is clearly visible. These shock-related spectra have two peaks near $St = 0.15$ and 0.3 . The first peak at $St = 0.15$ is has been associated with motion of the separation line [23], the second peak at is the strongest for $M = 0.7$, while the first peak become stronger at $M = 0.8$. This indicates a coupling or locking-in of the shock and separation line at high transonic speeds; this lock-in mechanism was also observed in relevant tunnel tests at transonic speeds [5]. Wake-related spectra at $\alpha = 125$ degrees for range of Mach numbers are shown in Figure 26, right, and exhibit self-similar behavior with a peak at higher frequency of around $St_D = 1.3$. Thus, the presence of shock does not affect shear-layer-type structures in the separation region.

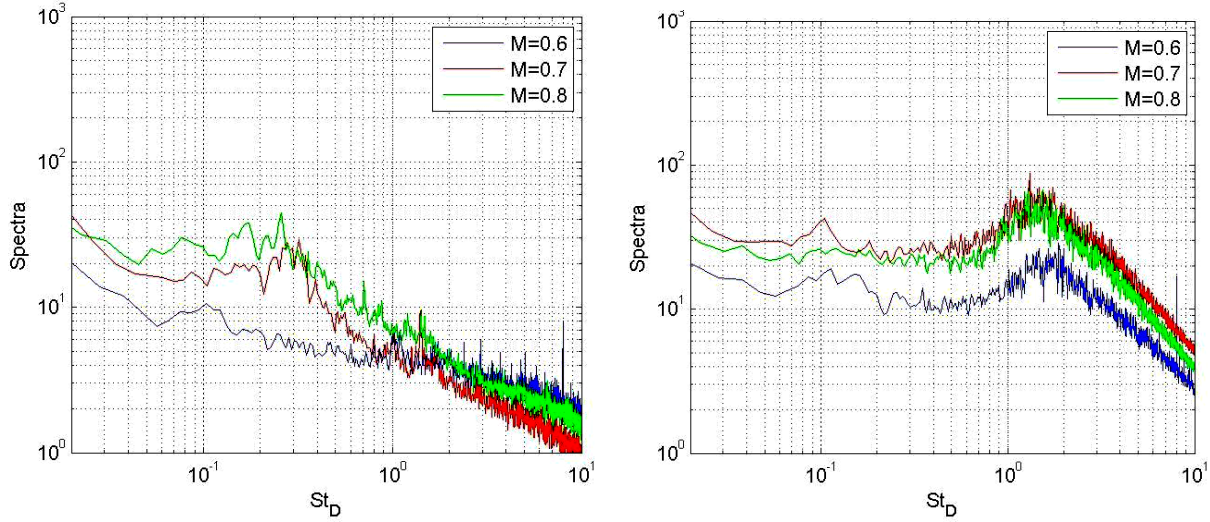


Figure 26. Normalized, aperture averaged wavefront spectra for $\alpha = 90$ degrees, left, and $\alpha = 125$ degrees, right, for incoming $M = 0.6, 0.7$ and 0.8 .

Pressure Results. The Optical results were presented in a previous Section; however here the data are augmented to compare with unsteady pressure data with temporal evolution of the wavefronts. The root mean square of the pressure coefficient is shown in Figure 27 for several Mach numbers. On the left is data from points at an elevation angle near 45° and on the right is data near 21° . For the higher transonic Mach numbers, there is a peak value at a viewing angle of 90° , where the unsteady shock is located. Similar Cp,RMS results were found during wind tunnel testing [23]. At the higher elevation points there is also an increase in the RMS near a viewing angle of 70° , which does not appear at lower elevation angle. In the full paper this will be looked into with more detail, but it is believed that it is likely due to the small trunnion gaps on the hemisphere surface. The higher elevation points correspond to data sets where the turret azimuthal angle is near 90° and the gaps are perpendicular to the flow, whereas the lower elevation angle data corresponds to sets where the gaps are parallel to the flow.

The pressure spectra at $\alpha = 90^\circ$, depicted in Figure 28, have peaks around $St = 0.15$ for all Mach numbers. The amount of energy at the peak Strouhal number increases as Mach number increases, particularly between Mach 0.7 and 0.8. This has been shown in previous studies to be the Strouhal number for the separation line motion [22] and for the unsteady shock at high transonic Mach numbers [20].

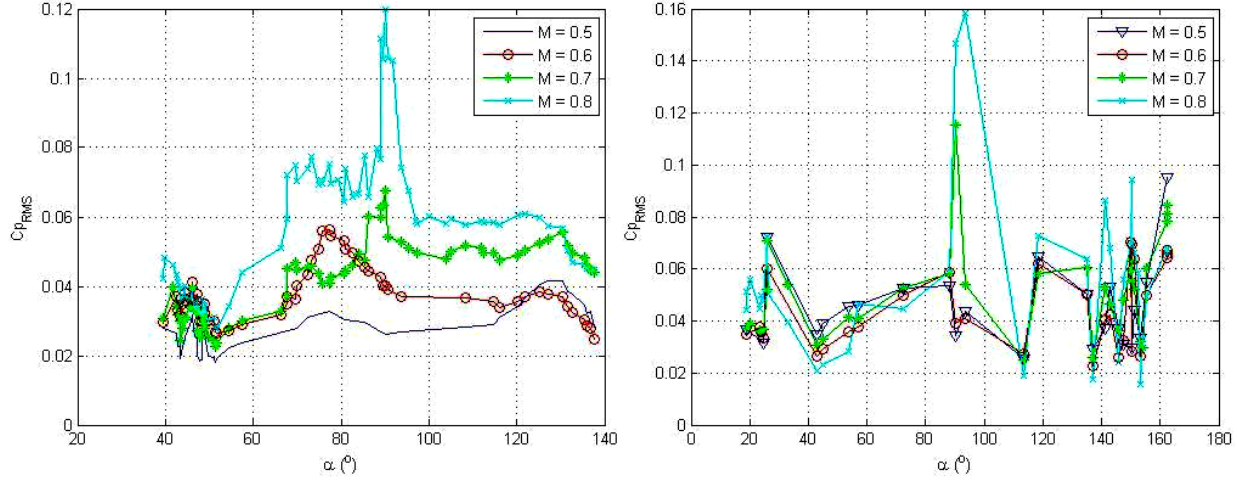


Figure 27. $C_p,_{RMS}$ vs viewing angle on the hemisphere for varying Mach number with $El = 45^\circ$, left, and $El = 21^\circ$, right.

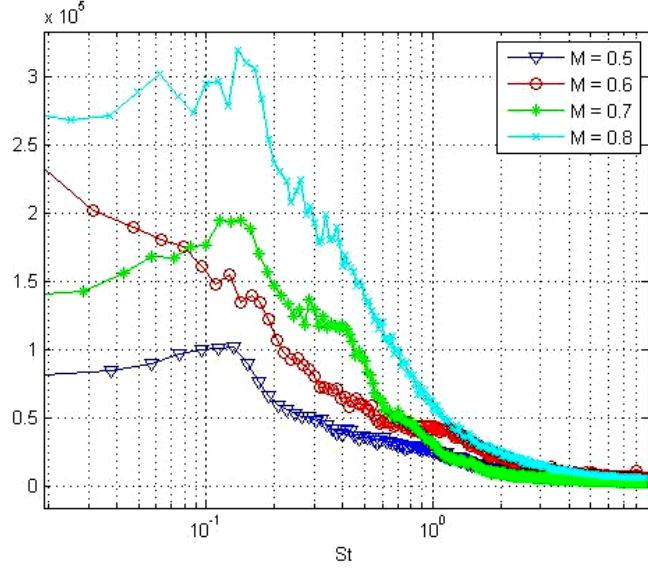


Figure 28. Pressure spectra for varying Mach number at $\alpha = 90^\circ$.

Figure 29 shows the mean removed spatial-temporal pressure field near a viewing angle of 90 degrees at a Mach number of 0.8. There are peaks and troughs near the viewing angle 90° due to the shock motion. The pressure fluctuations do not appear to be pure periodic, and have a time scale is similar to that of the optical shock motion measured for a hemisphere-on-cylinder configuration at the same Mach number [20].

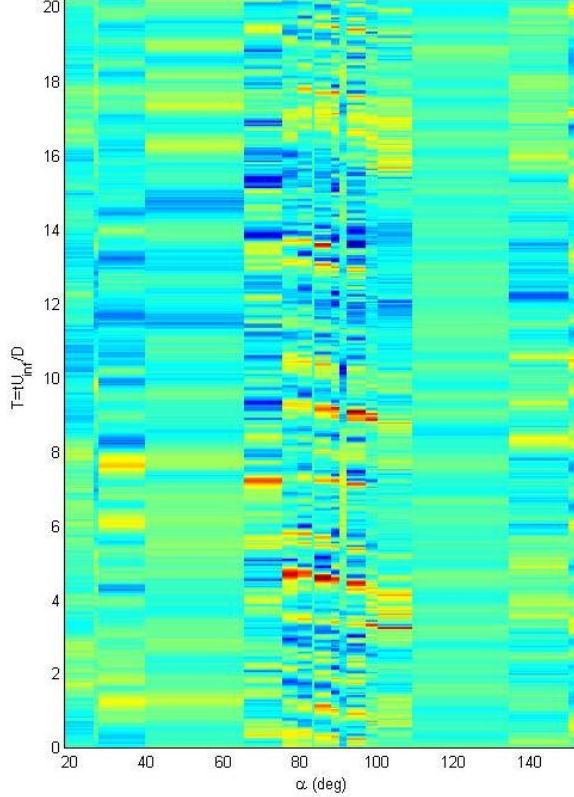


Figure 29. Mean removed spatial-temporal pressure field for $M = 0.8$.

V. HIGH-FIDELITY COMPUTATIONS OF AERO-OPTICS

Aero-Optics of 3-D Turrets. Large-eddy simulations (LES) of hemisphere-on-cylinder turrets have continued over the past year with a focus on the effects of realistic turret geometric features and realistic Reynolds numbers on the flow and aero-optics. The simulations are performed using an unstructured-mesh LES code, Charles, developed by Cascade Technologies, Inc. [26]. A wall model was employed to reduce the severe near-wall grid resolution requirement and make the simulations more affordable.

A baseline simulation for the canonical smooth hemisphere-on-cylinder turret in Mach 0.4 flow at a reduced Reynolds number of 4.6×10^5 (approximately 1/5 of the flight value) was previously examined [27]. It showed that the LES under-predicted the magnitude of the normalized OPD_{rms} when compared to AAOL experimental measurements at off-centerline viewing angles. To investigate the cause of this discrepancy, realistic geometric features like the gaps and ‘smiles’ that exist in the AAOL turret have been introduced into simulations.

In the past year the flow over a conformal turret with trunnion gaps aligned with flow direction was simulated at the reduced Reynolds number using approximately 61 million computational cells [28]. From the calculation, it was shown that the pressure difference on the turret surface drives flow from the front of the turret and redirects it to the top through the gaps (see Figure 30). This jetting effect causes an increase in density fluctuations near the aperture region as the jetted flow is convected into the turbulent wake. This leads to an increase in OPD_{rms} across all backward-viewing angles with larger differences seen at higher elevation angles as shown in Figure 31. The presence of the trunnion gaps also alters the spatial characteristics of the wavefronts in the Proper Orthogonal Decomposition (POD) modes presented in Figure 32. As POD decomposes data into modes ranked in terms of “energy” content, regions of the aperture affected by the gaps become

more important when they are compared with the baseline case. These results imply that in the development of adaptive-optic methods using similar data decompositions, the effect of viewing-angle dependent turret surface features (like gaps) may need to be taken into account as they can change the spatial structures of wavefronts.

Along with aero-optics, the effect of the gaps on the wake dynamics and the unsteady pressure on the surface of the turret are being investigated. Turrets with different gap orientations relative to the flow are also being simulated to find the effect of gaps in other configurations where the jetting may be less prevalent but can cause other flow separation and boundary layer effects.

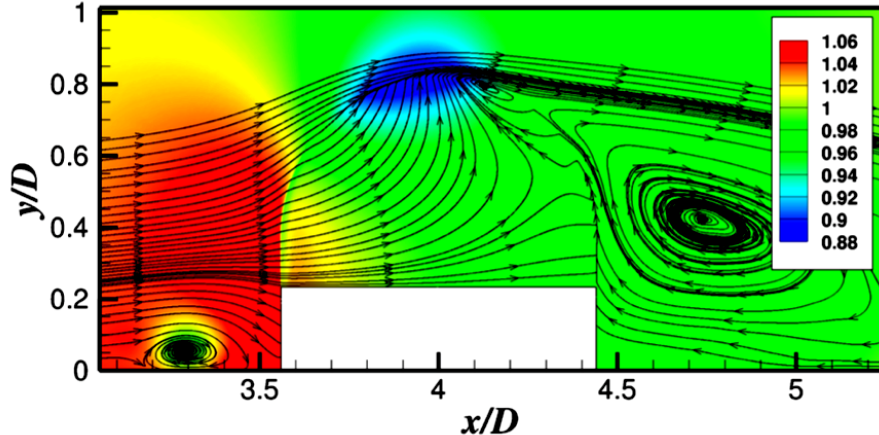


Figure 30. Streamlines of the time-averaged velocity in the mid-plane of the gap at $z = 0.236D$ showing the flow path through the turret gaps. Colored contours are of p/p_∞ .

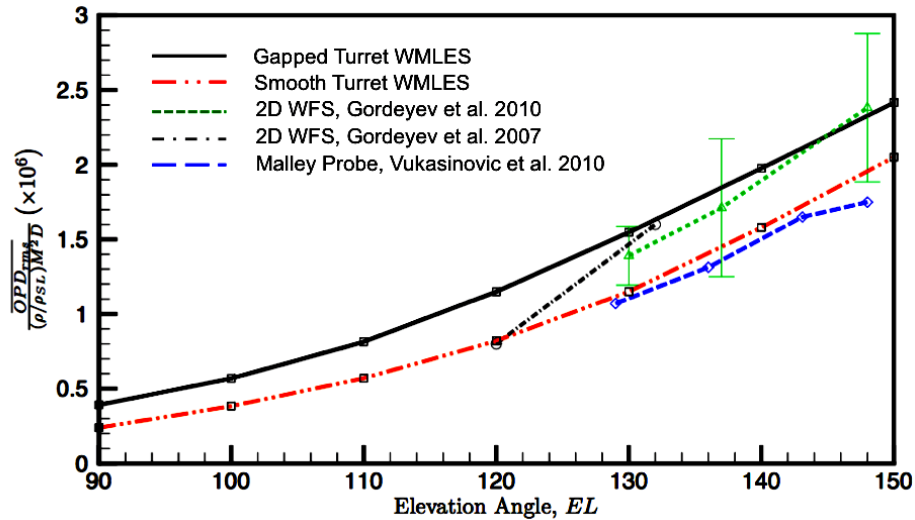


Figure 31. Normalized mean $\overline{\text{OPD}}_{\text{rms}}$ in the turret wake: Simulation values with and without gaps present.

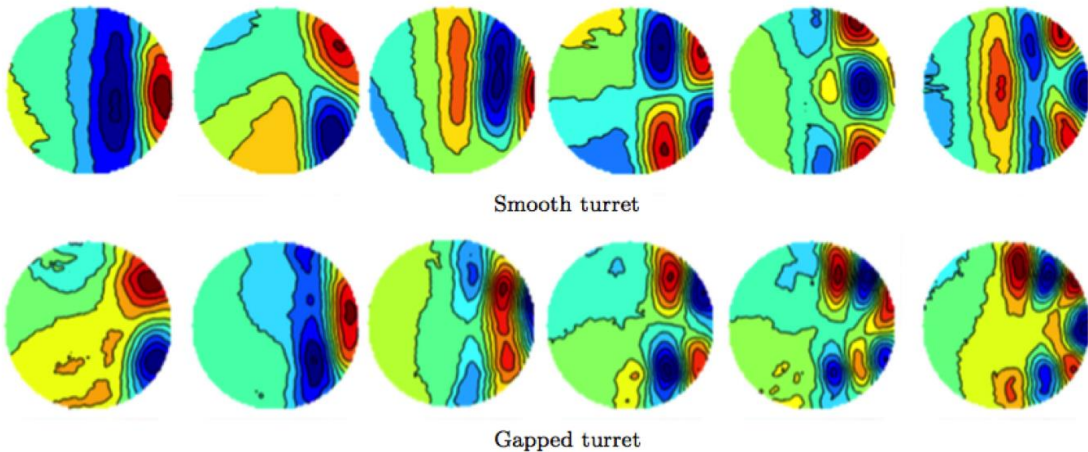


Figure 32. First six POD modes of smooth and gapped turret at an elevation angle of 120°. POD mode rank is descending from left to right.

The 3-D turret simulations are computationally very expensive, and efforts have been made to acquire external computational resources to support AAOL-T computations. Edwin Mathews, the graduate students who carried out the 3-D turret simulations, was awarded a prestigious Blue Waters graduate fellowship from the National Science Foundation, which provided two million core hours on the Blue Waters Supercomputing facility in FY 2014-15. A comparable allocation has been awarded for FY 2015-16. Using these resources a comprehensive study of the smooth conformal turret at the full Reynolds number of 2.3×10^6 was performed. The highly refined mesh contains over 200 million computational cells and this simulation is the largest numerical computation of a hemisphere-on-cylinder turret to date, providing unprecedented insight into the canonical turret flow. Visualizations of vortex structures, fluctuating density, and fluctuating pressure that show the complexity of the turret wake are displayed in Figure 33.

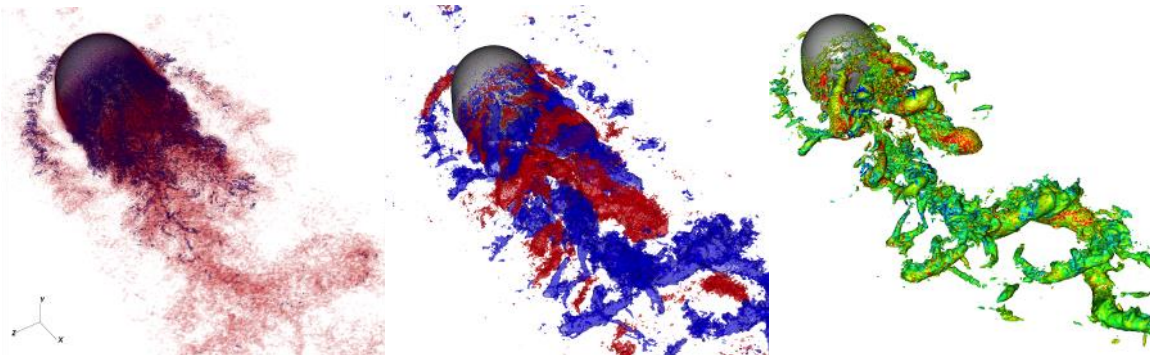


Figure 33. Visualizations of lambda 2 (vortex identification method), fluctuating density, and fluctuating pressure in the turret wake from the full Reynolds number simulation.

Utilizing the I/O capabilities of Blue Waters and data mining techniques, the aero-optics and fluid mechanics over the entire turret field of regard will be thoroughly investigated. The simulation generated a database of over 100 Terabytes of flow and optical data that will be used to gain key insights into the link between global flow phenomena and optical distortions. Simulation results for the pressure coefficient and optical distortion magnitude compare well with experimental measurements, as shown in Figure 34, and will be used in the near future to compare with results from the AAOL.

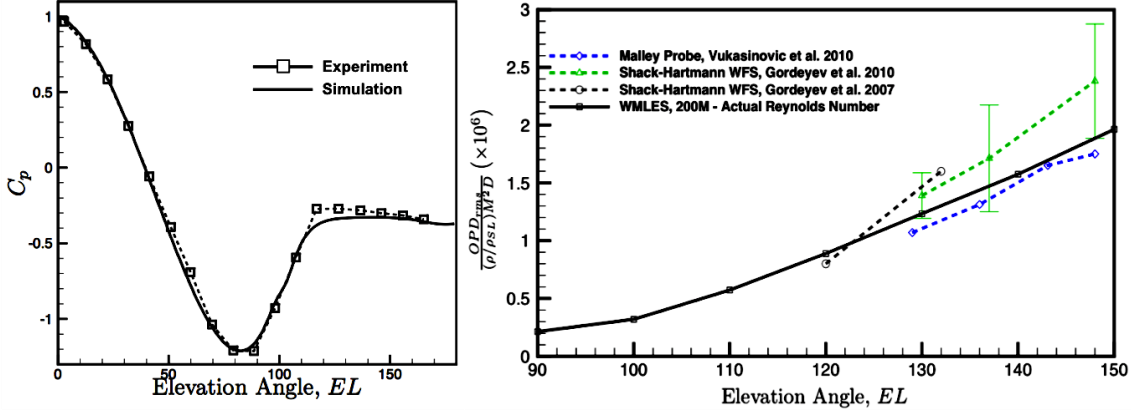


Figure 34. Pressure coefficient and normalized OPD_{rms} along the centerline of the turret compared with experimental measurements.

Turbulent Boundary Layers. To evaluate the accuracy of wall-modeled LES for aero-optical predictions and extend this method to transonic and supersonic flows, canonical configurations including subsonic and supersonic boundary layers and a 2-D cylindrical turret have been considered. The turbulent boundary layers are simulated at subsonic and supersonic speeds over a wide range of high Reynolds numbers. The simulation set-up is depicted schematically in Figure 35. The computational domain size is $45\delta \times 15\delta \times 3.1\delta$, where δ is the boundary layer thickness at the aperture center. With grid resolutions of $\Delta x = 0.05\delta$, $\Delta z = 0.032\delta$ and $\Delta y_{min} = 0.01\delta$ in streamwise, spanwise and wall-normal directions, respectively, the computational mesh contains 9 million cells.

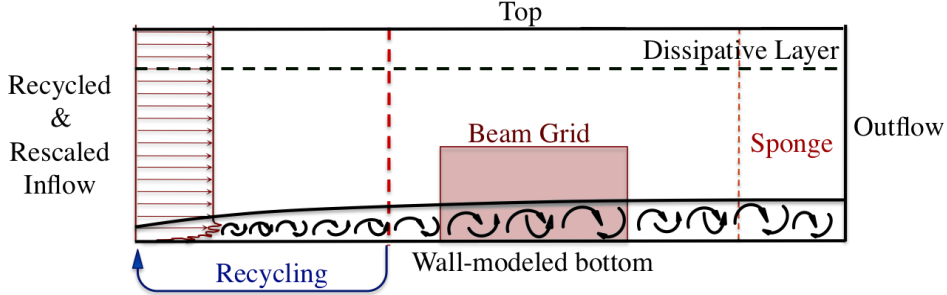


Figure 35. Schematic of the computational set-up for turbulent boundary layers.

Subsonic boundary layers are simulated at $M_\infty = 0.5$ and a range of momentum-thickness Reynolds numbers Re_θ from 2800 to 31000. In comparison with the wall-resolved LES of Wang and Wang [29] at $Re_\theta = 3550$, the computational expenses are reduced by two orders of magnitudes due to the application of a wall model. The basic flow statistics are shown in Figure 36. The mean velocity profiles show good agreement with the logarithmic law. The root-mean-square (rms) values of the streamwise velocity fluctuations are also in reasonable agreement with the experimental measurements of DeGraaff and Eaton [30] at $Re_\theta = 2900, 5200, 13000$ and 31000, which are the closest matches to the Reynolds numbers in the simulations.

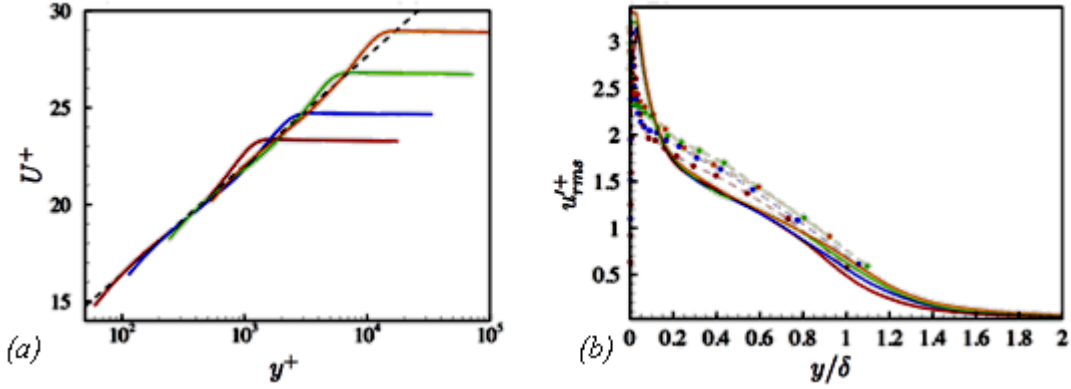


Figure 36. Streamwise velocity statistics in Mach 0.5 turbulent boundary layers: (a) Mean velocity profiles; (b) rms of streamwise velocity fluctuations. Wall-modeled LES: —, $Re_\theta = 2800$; —, $Re_\theta = 5600$; —, $Re_\theta = 13000$; —, $Re_\theta = 31000$. Experimental measurements of DeGraaff and Eaton [5]: -•-, $Re_\theta = 2900$; -•-, $Re_\theta = 5200$; -•-, $Re_\theta = 13000$; -•-, $Re_\theta = 31000$. ---, logarithmic law.

Simulations of supersonic boundary layers are conducted at $M_\infty = 1.7, 2.0$ and 3.0 , with $Re_\theta = 5.0 \times 10^4, 6.9 \times 10^4$, and 5.0×10^4 , respectively. The first case matches the experimental parameters of Souverein et al. [31] whereas the last two cases correspond to the experimental conditions of Gordeyev et al. [32, 33]. As shown in Figure 37, the predicted Van Driest transformed mean velocity profiles match the logarithmic law very well, and the rms values of streamwise velocity fluctuations at $M = 1.7$ and $Re_\theta = 5.0 \times 10^4$ show a reasonable agreement with the experimental data of Souverein et al. [31].

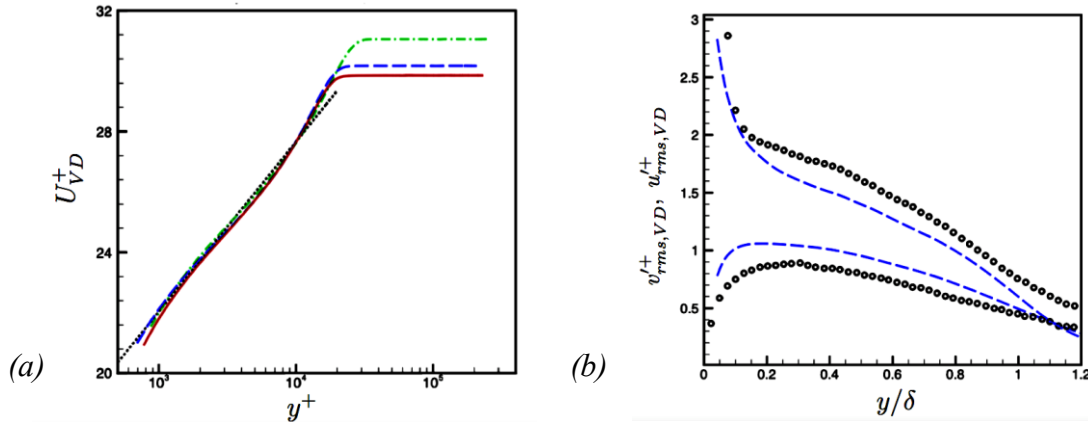


Figure 37. Van Driest transformed velocity statistics: (a) Mean streamwise velocity; (b) rms of streamwise and wall-normal velocity fluctuations. —, $M_\infty = 1.7, Re_\theta = 5.0 \times 10^4$; -·-, $M_\infty = 2.0, Re_\theta = 6.9 \times 10^4$; —, $M_\infty = 3.0, Re_\theta = 5.0 \times 10^4$; ○, experimental measurement of Souverein et al. at $M_\infty = 1.7$ and $Re_\theta = 5.0 \times 10^4$; ---, logarithmic law.

Figure 38 compares the normalized OPD_{rms} at free-stream Mach numbers $M_\infty = 0.5, 2.0$ and 3.0 with experimental measurements and the prediction by a model (ND model) developed by Gordeyev et al. [33]. The wall-modeled LES results show the correct trend and reasonable

agreement with experimental data at these three Mach numbers, but the rate of change with Mach number deviates from the experimental measurements. The sources of the discrepancy are currently under investigation.

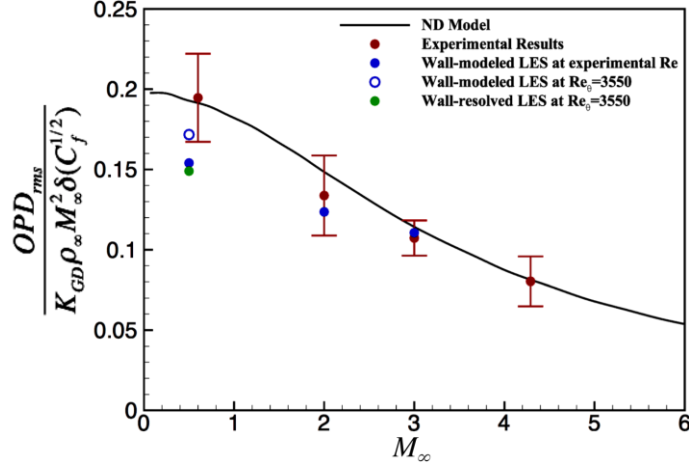


Figure 38. Normalized aero-optical distortion magnitude for turbulent boundary layers.

Subsonic Flow over a Cylindrical Turret with a Flat Window. The flow over a cylindrical turret with a flat window has been simulated under the same conditions as in the experiment of Gordeyev et al. [34]: $M = 0.5$ and $Re_R = 5.6 \times 10^5$ based on the turret radius R . As shown schematically in Figure 39, the computational inlet is located $2.75R$ upstream of the turret axle, and the elevation angle of the turret is fixed at 120° . The inflow turbulence data are generated by a separate flat-plate boundary layers simulation. The inlet boundary-layer thickness δ_{in} is approximately $0.14R$ and the momentum-thickness Reynolds number is $Re_\theta = 7650$. The domain size is $12.6R \times 2.81R \times 0.422R$. This wall-modeled LES at the *full* experimental Reynolds number employs a mesh with only 4.9 million grid cells. The computational expense is approximately 10% of that of the wall-resolved LES by Wang et al. [35], which was performed at 16% of the experimental Reynolds number. The computed velocity and density statistics at four streamwise locations above the optical window are compared to the experimental measurements and wall-resolved LES results. As can be seen in Figures 40 and 41, reasonable agreement is obtained.

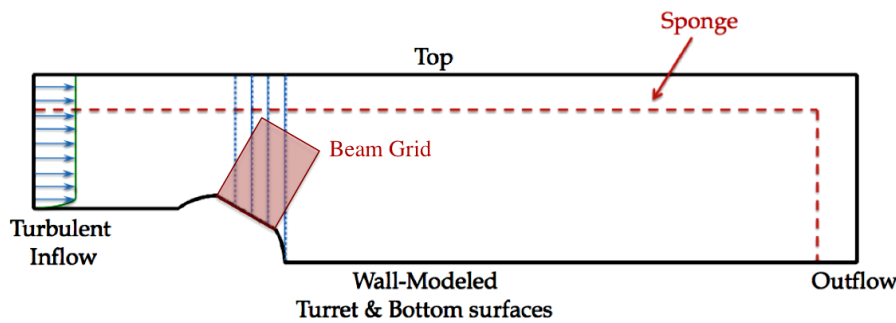


Figure 39. Schematic of the computational set-up for subsonic flow over a cylindrical turret with a flat window. Dashed blue lines are the locations where comparisons are made with the experimental data and previous simulation results.

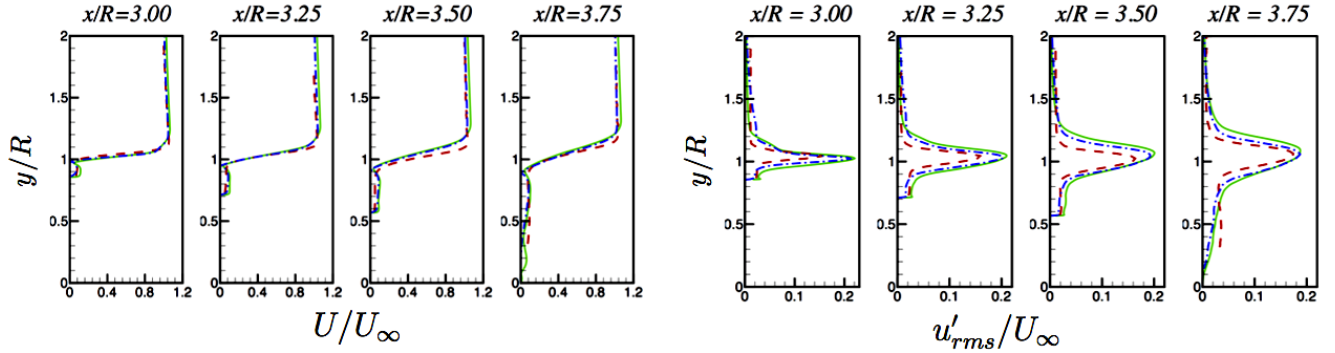


Figure 40. (a) Mean streamwise velocity profiles and (b) rms of velocity fluctuations at four locations above the optical window: —, wall-modeled LES; -·-, wall-resolved LES of Wang et al. [10] at a reduced Reynolds number; -·-, experiment of Gordeyev et al. [35].

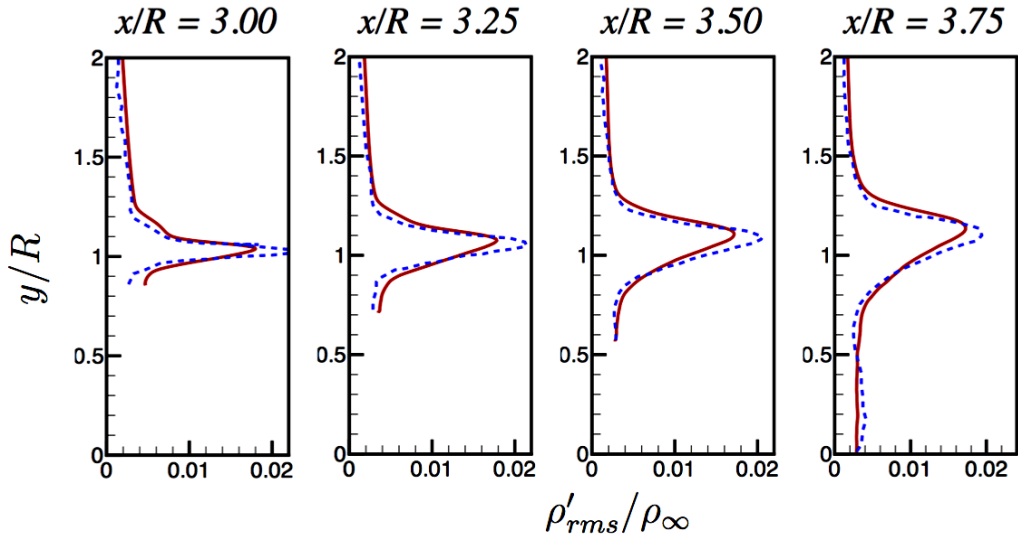


Figure 41. Density fluctuations above the optical window: —, wall-modeled LES; -·-, wall-resolved LES at a reduced Reynolds number.

An aperture size of $1.0R \times 0.422R$ is employed for optical calculation. The time-averaged OPD_{rms} from the wall-modeled LES is $7.17 \times 10^{-7} R$, which agrees well with the value of $7.10 \times 10^{-7} R$ from the wall-resolved LES and is approximately 10% higher than the experimentally measured value of $6.39 \times 10^{-7} R$.

Transonic Flow over a Cylindrical Turret with a Conformal Window. The experiment of Vorobiev et al. [5] is being simulated by using wall-modeled LES. The computational set-up in the x - y plane is illustrated in Figure 42. Time-dependent turbulent inflow at $M_{in} = 0.68$ and $Re_{\theta,in} = 10^4$, which match the experimental parameters, is fed into the simulation domain, and the back pressure in the simulation is determined iteratively to match the experimental mean pressure measured in the wind tunnel. The current mesh consists of 15 million cells. In Figure 43, the numerical schlieren is displayed along with shadowgraphs from the experiment. These preliminary results show qualitative agreement with experimental observations in terms of different patterns of shock/wake dynamics as the back pressure is decreased from 98% to 77% of the inlet static pressure. The

simulations are ongoing and will be validated against experimental measurements, and optical distortions and their relation to the shock dynamics will be investigated.

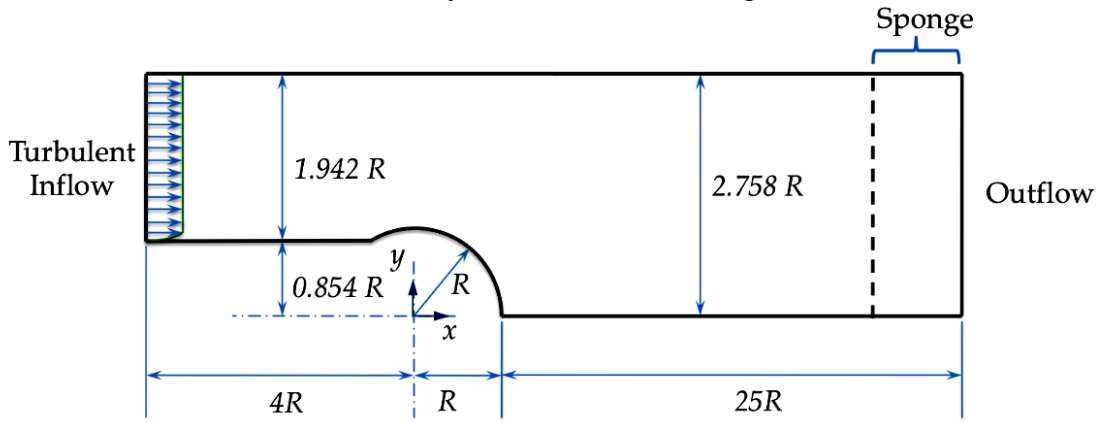


Figure 42. Schematic of the computational set-up for transonic flow over a cylindrical turret with a conformal window. Dimensions are presented in terms of turret radius R .

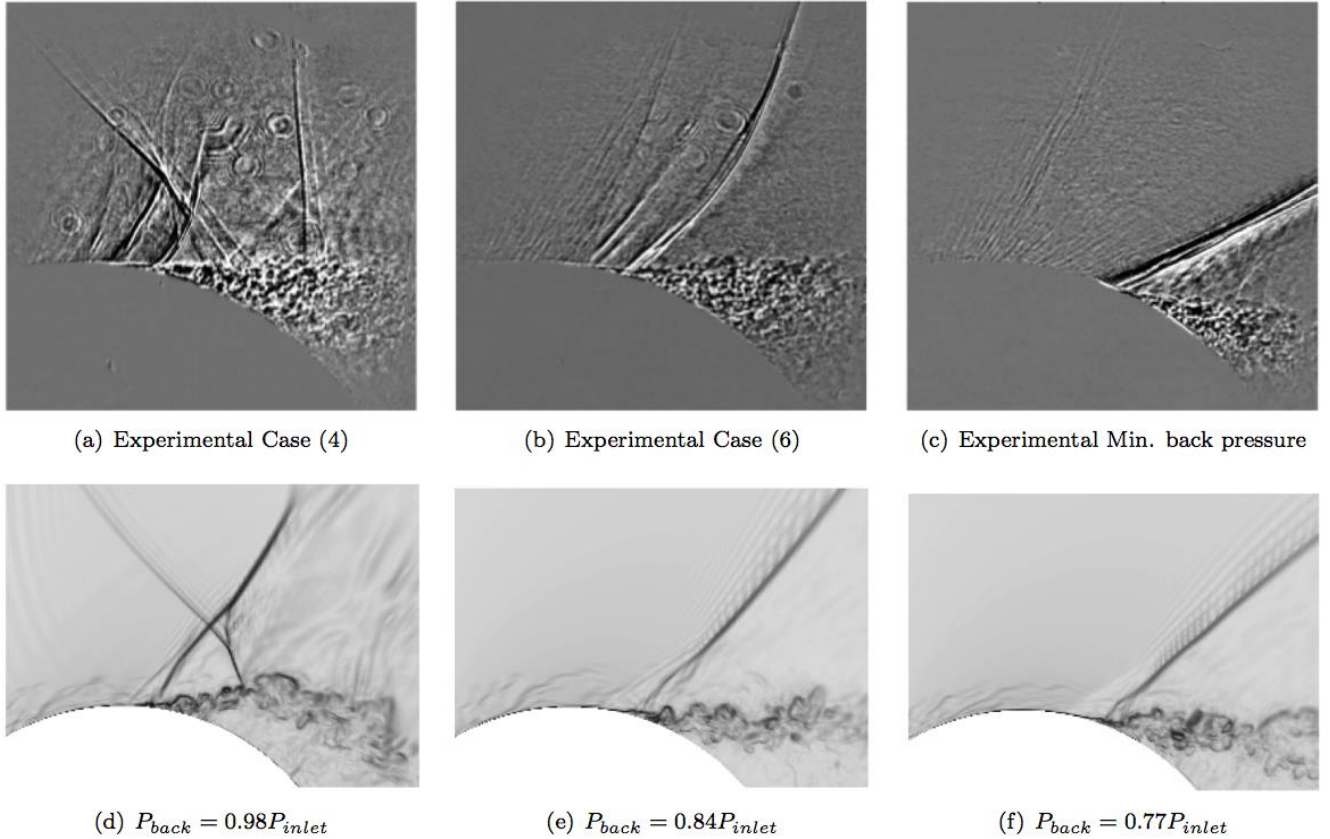


Figure 43. A qualitative comparison between the shadowgraphs (a, b and c) of the experiment conducted by Vorobiev et al. [11] and the numerical schlieren (NS=0.8 $\exp[10(|\nabla\rho| - |\nabla\rho|_{\min}) / (|\nabla\rho|_{\max} - |\nabla\rho|_{\min})]$) of the current simulations at different back pressures (d, e and f).

VI. ADVANCES IN PREDICTIVE AERO-OPTIC CONTROL

A challenge to the implementation of real-time adaptive optic systems on aircraft is the latency problem [36]. Frequencies associated with dominant aero-optic aberrations are typically on the order of hundreds or thousands of kilohertz for practical applications. Small delays in an adaptive-optic feedback controller can cause substantial performance degradation or even instability. The source of this delay is the cumulative latency in digital processing; input/output communication between deformable mirrors, sensors, and processors; and dead-time in mechanical system response. Dead-time is conventionally viewed as a difficult problem to deal with in feedback control [37]: regardless of the quality of a controller, the controller fundamentally cannot respond to a sensed disturbance for at least the duration of the cumulative dead time. The effect of this is to put an upper limit on controller performance and bandwidth.

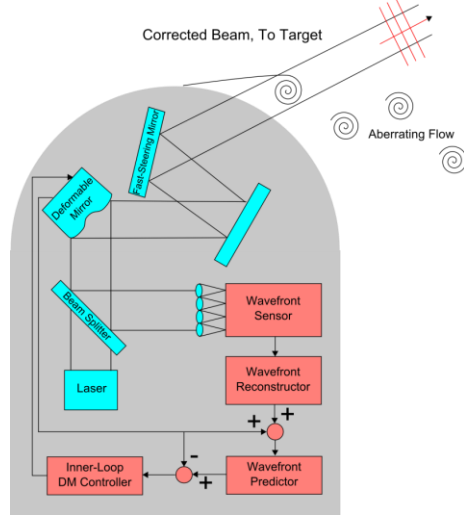


Figure 44. Feedforward system architecture [36]

One method for overcoming this obstacle is to use a *feedforward* predictor in conjunction with a feedback controller. This feedforward element uses prior knowledge of disturbance dynamics to predict the evolution of an aberrating flow over a short temporal horizon, equal to the cumulative feedback controller delay. The improved control architecture is shown in Figure 44. Since aero-optic applications typically involve hundreds of subapertures, it is desirable to reduce the dimensionality of the prediction problem. A method was investigated this year that relies on model reduction using Proper Orthogonal Decomposition [38] and a neural network [39] to predict the temporal evolution of the POD coefficients.

To analyze performance of this proposed system, we divided the flow into three general regions depending on viewing angle, α . For $\alpha < 90$ deg., the flow is fully attached and the resulting aero-optical aberrations are not severe. Between 90 and 120 degrees we begin to witness the onset of separation, and the optical aberrations begin to become larger. At viewing angles of 120 degrees and larger, the flow becomes fully separated and the aero-optical aberrations become very large. Fortunately, we have discovered that the fully separated flow has more predictable behavior that approximates a shear layer: that is, the most optically-active region is also the easiest to predict. This means that a predictive controller will actually perform better for the flow region with the worst aberrations, which is a favorable characteristic. We simulated a closed-loop adaptive-optic control system operating at 25 kHz (equivalent to the wavefront sensor sample rate of the flight test data). In the separated region, we achieved approximately -3.5dB (about 55%) wavefront

disturbance rejection for small amounts (1 timestep, or 40 μs) of latency, and about -2dB (about 35%) wavefront disturbance rejection for larger amounts (5 timesteps, or 200 μs) of latency.

Since this paper was published early this year, we have developed an updated prediction model that is computationally less intensive as well as more robust and accurate. Like the neural network model, it relies on prior knowledge of flow behavior to make predictions; however, it is purely linear and thus its stability characteristics may be more easily understood.

We may decompose each wavefront at timestep k , \mathbf{v}_k , into a summation of POD modes, Φ_n , multiplied by corresponding temporal coefficients x_k , as follows,

$$\mathbf{v}_k = \sum_{n=1}^N x_n(k) \Phi_n .$$

To perfectly reconstruct a wavefront, the POD modes must span the entire set if the training matrix is full rank. In general, this will be true for experimental data, although the highest-order modes are likely contaminated with noise. Thus, the value for N will be equal to the number of subapertures in the wavefront matrix for a perfect reconstruction. In practice, it is desirable to truncate the set of modes used for reconstruction to reduce noise and reduce computational requirements for the prediction model. In general, the low-order POD modes will capture the motion of coherent turbulent structures across the optical aperture.

The goal for the coefficient prediction function, \mathbf{g} , is to estimate future POD coefficients based on the past M measurements while minimizing the norm of the prediction residual error, $\mathbf{\epsilon}_{k+1}$,

$$\mathbf{v}_{k+1} = \Phi_1^N \mathbf{g}(\mathbf{x}_k, \mathbf{x}_{k-1}, \dots, \mathbf{x}_{k-M+1}) + \mathbf{\epsilon}_{k+1} .$$

The coefficient prediction is then multiplied by the POD modes to obtain the full wavefront prediction, \mathbf{v}_{k+1} . For multi-step prediction, this function is used recursively.

We found a practical prediction limit of about 16 POD modes using the POD/neural network method. Beyond this number of modes, the improvement in prediction accuracy diminished so rapidly that the extra computational requirements were not really justifiable. With the more stable and accurate linear predictor, we have observed consistently better performance up to about 64 modes.

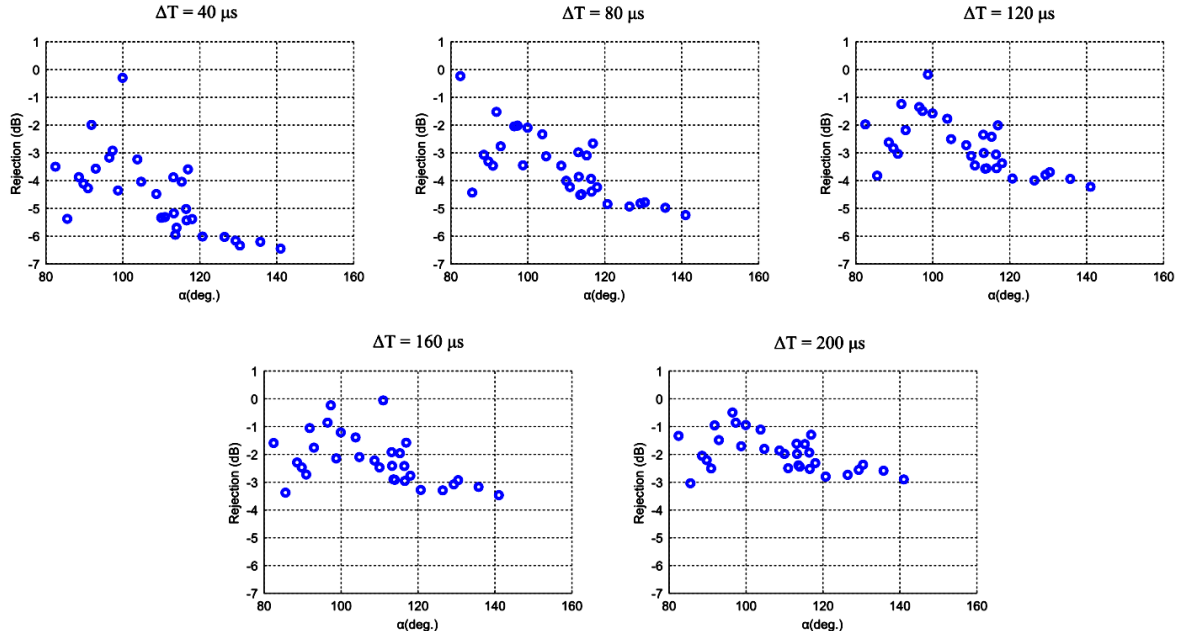


Figure 45: Simulated mean disturbance rejection using flight test data for varying amounts of latency, assuming a 25kHz control loop

The resulting error rejection functions are shown in Figure 45**Error! Reference source not found.** for varying amounts of latency. Up to -6.5 dB (or 78%, compared to -3.5 dB or 55% previously) of error rejection are seen for small amounts of latency. For larger amounts of latency, we observe up to -3dB (or 50%, compared to -2dB or 35%) of rejection.

Future work will focus on improving the quality of the predictions, as well as methods to improve the robustness of the method as the flow condition slowly changes as a function of Mach number, altitude, viewing angle, etc. These improvements are important, because system performance approximately degrades with RMS wavefront error *squared*. This is illustrated in Figure 46**Error! Reference source not found.**. For example, a -3dB wavefront error reduction corresponds to a taking an uncorrected Strehl Ratio of 0.2 to 0.67.

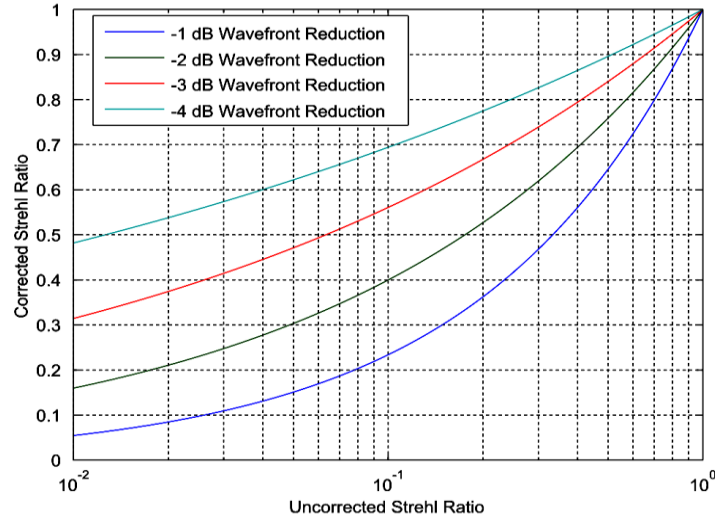


Figure 46: Corrected and uncorrected Strehl ratios as a function of mean wavefront error reduction

VII. CONCLUDING REMARKS

Please keep in mind that this report reflects only the highlights of what we accomplished in the third year of this grant; not included is, for example, the efforts undertaken to support the DARPA/AFRL 40% ABC turret except for a short mention that we are doing this. The work on adaptive optics was only touched on; since this work is still very much in progress, I intend to give a more detailed report on this area in next year's report. Even so, it is clear that the grant has been extremely productive.

This effort has at least partially supported 5 faculty, 1 research specialist, 2 post-doctoral fellows, 1 research staff, and 10 graduate students.

REFERENCES

- [1] E Jumper, M Zenk, S Gordeyev, D Cavalieri and M. Whiteley, "Airborne Aero-Optics Laboratory", *Journal of Optical Engineering*, **52**(7), 071408, 2013.
- [2] C. Porter, S. Gordeyev, M. Zenk and E. Jumper, "Flight Measurements of the Aero-Optical Environment around a Flat-Windowed Turret", *AIAA Journal*, Vol. 51, No. 6, Jun. 2013, pp. 1394-1403.
- [3] N. De Lucca, S. Gordeyev and E.J. Jumper, "In-flight aero-optics of turrets", *Journal of Optical Engineering*, **52**(7), 071405, 2013.

- [4] R. Burns, S. Gordeyev, E. Jumper, S. Gogineni, M. Paul and D.J. Wittich, "Estimation of Aero-Optical Wavefronts Using Optical and Non-Optical Measurements ", AIAA Paper 2014-0319, 2014.
- [5] A. Vorobiev, S. Gordeyev, E. Jumper, S. Gogineni, A. Marruffo and D.J. Wittich, "Low-Dimensional Dynamics and Modeling of Shock-Separation Interaction over Turrets at Transonic Speeds", AIAA Paper 2014-2357, 2014.
- [6] S. Gordeyev and E. Jumper, "Fluid Dynamics and Aero-Optics of Turrets", *Progress in Aerospace Sciences*, **46**, (2010), pp. 388-400.
- [7] N. De Lucca, S. Gordeyev, E. Jumper and D.J. Wittich, "Aero-Optical Environment around Turrets at Forward-Viewing Angles", AIAA Paper 2013-0721, 2013.
- [8] R. Jelic, S. Sherer and R. Greendyke, "Simulation of Various Turret Configurations at Subsonic and Transonic Flight Conditions Using OVERFLOW", *Journal of Aircraft*, **50**, pp. 398-409, 2013.
- [9] Courier, W.J., Whiteley, M., Goorskey, D.J., Drye, R., Barber, J., Stutts, J. and Porter, C., "Aero-Optical Evaluation of Notional Turrets in Subsonic, Transonic and Supersonic Regimes", AIAA Paper 2014-2355, 2014.
- [10] Jumper, E.J., Gordeyev, S., Cavalieri, D. and Rollins, P. "Airborne Aero-Optics Laboratory - Transonic (AAOL-T)," AIAA Paper 2015-0675, 2015.
- [11] S. Gordeyev, N. De Lucca, E. Jumper, K. Hird, T.J. Juliano, J.W. Gregory, J. Thordahl and D.J. Wittich, "Comparison of Unsteady Pressure Fields on Turrets with Different Surface Features using Pressure Sensitive Paint ", *Experiments in Fluids*, **55**, p. 1661, 2014.
- [12] N. De Lucca, S. Gordeyev and E.J. Jumper, "Global Unsteady Pressure Fields Over Turrets In-Flight", AIAA Paper 2015-0677, 2015.
- [13] Goorskey, D.J., Drye, R. and Whiteley M.R., "Dynamic modal analysis of transonic Airborne Aero-Optics Laboratory conformal window flight-test aero-optics," *Opt. Eng.* **52** (7), 071414, 2013.
- [14] M. Wang, A. Mani and S. Gordeyev, "Physics and Computation of Aero-Optics", *Annual Review of Fluid Mechanics*, **44**, pp. 299-321, 2012.
- [15] B. Vukasinovic, A. Glezer, S. Gordeyev, E. Jumper and V. Kibens, "Hybrid Control of a Turret Wake," *AIAA Journal*, **49**(6), pp. 1240-1255, 2011.
- [16] M. Palaviccini, L. Cattafesta and B. George, "Passive Flow Control over a Three-Dimensional Turret with a Flat Aperture", AIAA Paper 2011-3265, 2011.
- [17] D.S. Dolling, "Fifty years of shock-wave/boundary-layer interaction research: what next?", *AIAA Journal*, **39**(8), pp.1517–1531, 2001.
- [18] Green J.E. "Interaction between shock waves and boundary layers" *Progress in Aerospace Sciences*, **11**, pp. 235-340, 1970.
- [19] Delery J.M. "Shock wave/turbulent boundary layer interaction and control", *Prog. Aerospace Sci.*, **22**, pp. 209-280, 1985.
- [20] J. Morrida, S. Gordeyev, N. De Lucca, E. Jumper. "Aero-Optical Investigation of Transonic Flow Features and Shock Dynamics on Hemisphere-On-Cylinder Turrets", AIAA Paper 2015-0676, 2015.
- [21] E.J. Jumper, S. Gordeyev, D. Cavalieri, P. Rollins, M.R. Whiteley and M.J. Krizo, "Airborne Aero-Optics Laboratory - Transonic (AAOL-T)," AIAA Paper 2015-0675, 2015.
- [22] S. Gordeyev, N. De Lucca, E. Jumper, K. Hird, T.J. Juliano, J.W. Gregory, J. Thordahl and D.J. Wittich, "Comparison of Unsteady Pressure Fields on Turrets with Different Surface Features using Pressure Sensitive Paint ", *Experiments in Fluids*, **55**, p. 1661, 2014.
- [23] J. Morrida, S. Gordeyev, E. Jumper, "Investigation of Shock Dynamics on a Hemisphere Using Pressure and Optical Measurements", submitted to AIAA SciTech Conference, 2016.

- [24] Courier, W.J., Porter, C., Barber, J., Stutts, J., Whiteley, M., Goorskey, D. and Drye, R., "Aero-Optical Evaluation of Notional Turrets in Subsonic, Transonic and Supersonic Regimes," AIAA Paper 2014-2355, 2014.
- [25] R. Jelic, S. Sherer and R. Greendyke, "Simulation of Various Turret Configurations at Subsonic and Transonic Flight Conditions Using OVERFLOW", *Journal of Aircraft*, **50**, pp. 398-409, 2013.
- [26] Khalighi, Y., Nichols, J.W., Ham, F., Lele, S.K. and Moin, P., "Unstructured Large Eddy Simulation for Prediction of Noise Issued from Turbulent Jets in Various Configurations". AIAA Paper 2011-2886.
- [27] Mathews, E., Wang, K., Wang, M. and Jumper, E., "LES Analysis of Hemisphere-on-Cylinder Turret Aero-Optics". AIAA Paper 2014-0323.
- [28] Mathews, E., Wang, K., Wang, M., and Jumper, E., "Numerical Investigation of Aero-Optical Distortions over a Hemisphere-on-Cylinder Turret with Gaps". AIAA Paper 2015-3248.
- [29] Wang, K. and Wang, M., "Aero-Optics of Subsonic Turbulent Boundary Layers," *Journal of Fluid Mechanics*, Vol. 696, 2012, pp. 122–151.
- [30] DeGraaff, D. B. and Eaton, J. K., "Reynolds-Number Scaling of the Flat-Plate Turbulent Boundary Layer," *Journal of Fluid Mechanics*, Vol. 422, 2000, pp. 319–346.
- [31] Souverein, L. J., Dupont, P., Debièvre, J.-F., Van Oudheusden, B. W., and Scarano, F., "Effect of Interaction Strength on Unsteadiness in Shock-Wave-Induced Separations," *AIAA journal*, Vol. 48, No. 7, 2010, pp. 1480–1493.
- [32] Gordeyev, S., Jumper, E., and Hayden, T. E., "Aero-Optical Effects of Supersonic Boundary Layers," *AIAA journal*, Vol. 50, No. 3, 2012, pp. 682–690.
- [33] Gordeyev, S., Rennie, R. M., Cain, A. B., and Hayden, T. E., "Aero-Optical Measurements of High-Mach Supersonic Boundary Layers," AIAA Paper 2015-3246.
- [34] Gordeyev, S., Cress, J., Smith, A., and Jumper, E. J., "Improvement in Optical Environment over Turrets with Flat Window Using Passive Flow Control," AIAA Paper 2010-4492.
- [35] Wang, K., Wang, M., Gordeyev, S., and Jumper, E., "Computation of Aero-Optical Distortions over a Cylindrical Turret with Passive Flow Control," AIAA paper 2010-4498.
- [36] R. Burns, E. Jumper, and S. Gordeyev, "A Latency-Tolerant Architecture for Airborne Adaptive Optic Systems," *53rd Aerosp. Sci. Meet.*, 2015.
- [37] V. VanDoren, "Overcoming the deadtime dilemma," *Control Engineering*, vol. 44, no. 8, p. 120, Jun-1997.
- [38] G. Berkooz, P. Holmes, and J. L. Lumley, "The Proper Orthogonal Decomposition in the Analysis of Turbulent Flows," *Annu. Rev. Fluid Mech.*, vol. 25, no. 1, pp. 539–575, 1993.
- [39] K. Hornik, M. Stinchcombe, and H. White, "Multilayer Feedforward Networks Are Universal Approximators," *Neural Netw.*, vol. 2, no. 5, pp. 359–366, 1989.

AFOSR Deliverables Submission Survey

Response ID:7045 Data

1.

Report Type

Final Report

Primary Contact Email

Contact email if there is a problem with the report.

prollins@nd.edu

Primary Contact Phone Number

Contact phone number if there is a problem with the report

574-631-3755

Organization / Institution name

University of Notre Dame

Grant/Contract Title

The full title of the funded effort.

Airborne Aero-Optics Laboratory-Transonic (AAOL-T)

Grant/Contract Number

AFOSR assigned control number. It must begin with "FA9550" or "F49620" or "FA2386".

FA9550-13-1-0001

Principal Investigator Name

The full name of the principal investigator on the grant or contract.

Dr. Eric Jumper

Program Officer

The AFOSR Program Officer currently assigned to the award

Dr. John Luginsland

Reporting Period Start Date

10/15/2012

Reporting Period End Date

10/14/2015

Abstract

This report covers the third year of the Airborne Aero-Optics Laboratory-Transonic (AAOL-T) program. Aero-optics severely limits an airborne directed-energy system's lethal field of regard; aero-optics refers to the deleterious effect that the density fluctuations in the flow have on an airborne optical system. The AAOL-T program studies aero-optical aberration problems from experimental, theoretical and computational approaches; the most unique part of the program is that we also perform flight tests using Falcon 10's, capable of testing at greater than Mach 0.8. The program makes use of two aircraft, one to project a small-aperture, diverging beam toward an optical turret on the second, laboratory aircraft. The third year of the program has been productive with thirty-one flights flown in support of both the baseline program and to support AFRL/DARPA 40% ABC Turret testing, of which 5 flights plus seven at the end of September 2014 were under the baseline program. During the baseline program, extensive measurements of aero-optical environment around both hemisphere-on-cylinder and hemisphere-only turrets were performed for Mach range between 0.5 and 0.8. Fluidic environment was also studied in-flight by collecting simultaneous unsteady pressure data over an array of pressure sensors on the surface of these turrets for Mach between 0.5 and 0.8. In addition to collecting the aero-optical data in flight, the baseline data was

DISTRIBUTION A: Distribution approved for public release.

used in a wide range of analysis of these data and using the data to explore advanced techniques in adaptive optics. The report describes mainly analysis of data and the computational work done in year three of the program.

Distribution Statement

This is block 12 on the SF298 form.

Distribution A - Approved for Public Release

Explanation for Distribution Statement

If this is not approved for public release, please provide a short explanation. E.g., contains proprietary information.

SF298 Form

Please attach your [SF298](#) form. A blank SF298 can be found [here](#). Please do not password protect or secure the PDF. The maximum file size for an SF298 is 50MB.

[sf0298 AFOSR 202022 Oct 2016.pdf](#)

Upload the Report Document. File must be a PDF. Please do not password protect or secure the PDF . The maximum file size for the Report Document is 50MB.

[AAOL-T AFOSR Final Report Oct 2016.pdf](#)

Upload a Report Document, if any. The maximum file size for the Report Document is 50MB.

Archival Publications (published) during reporting period:

New discoveries, inventions, or patent disclosures:

Do you have any discoveries, inventions, or patent disclosures to report for this period?

No

Please describe and include any notable dates

Do you plan to pursue a claim for personal or organizational intellectual property?

Changes in research objectives (if any):

Change in AFOSR Program Officer, if any:

Extensions granted or milestones slipped, if any:

AFOSR LRIR Number

LRIR Title

Reporting Period

Laboratory Task Manager

Program Officer

Research Objectives

Technical Summary

Funding Summary by Cost Category (by FY, \$K)

	Starting FY	FY+1	FY+2
Salary			
Equipment/Facilities			
Supplies			
Total			

Report Document

Report Document - Text Analysis

Report Document - Text Analysis

Appendix Documents

DISTRIBUTION A: Distribution approved for public release.

2. Thank You

E-mail user

Oct 03, 2016 08:54:37 Success: Email Sent to: prollins@nd.edu